ELECTRICAL ENGINEERING AND ENERGY

OPEN ACCESS

Bidirectional Wireless Power Transfer for Vehicle-to-Grid Services: Converter Control, Power Quality and Grid-Interface Behaviour

Victor Ogunyemi[1] and Taofeek Lawal[1]

[1]Department of Electrical and Electronics Engineering, Olabisi Onabanjo University, Ago-Iwoye, Ogun State, Nigeria

Submitted: 11 October 2026
Accepted: 16 November 2026
Published: 23 November 2026

Corresponding author,
Victor Ogunyemi
ogunyemivictor738@gmail.com

DOI: 10.64470/elene.2026.51

RESEARCH ARTICLE

Copyright, Authors, Distributed under Creative Commons CC-BY 4.0

Abstract: Bidirectional wireless power transfer lets parked electric vehicles provide vehicle-to-grid (V2G) services without a plug, but its converter control and grid-interface behaviour have rarely been studied together. This paper presents a simulation-based study of a 7.7-kW, 85-kHz double-sided inductor-capacitor-capacitor (LCC) wireless charger connected to a 230-V, 50-Hz single-phase grid through an LCL-filtered active front end. A fundamental and multi-harmonic model of the wireless link is derived and cross-checked against 240 switching-level MATLAB/Simulink operating points (mean power error 0.26%, maximum 3.5%). Single-, dual- and zero-voltage-switching (ZVS)-constrained triple-phase-shift (SPS, DPS, TPS) modulation are synthesised by optimisation and embedded in a cascaded controller with a second-order-generalised-integrator-phase-locked loop (SOGI-PLL), DC-link power feed-forward, proportional-resonant current control and IEEE Std 1547-2018 frequency-watt and volt-var functions. With SPS, the grid-to-battery efficiency at 1.54 kW is 69.8% (charging) and 59.7% (V2G); DPS and TPS raise it above 90% and reach 91.8%–92.2% at rated power, TPS avoiding hard switching at every simulated point, with partial ZVS at some edges. The charger reverses its ±7.7-kW range within 22 ms at the grid, keeps the current total demand distortion (TDD) below 0.8% with a distorted grid voltage, follows the frequency-watt droop within 40 ms and supplies four-quadrant reactive power without cycling the battery. On a weak feeder, volt-var control moves the voltage from 0.930 to 0.945 p.u. in charging and from 1.050 to 1.041 p.u. in V2G, provided the grid-voltage feed-forward is limited to the fundamental. The simulations indicate that a bidirectional wireless charger with variable-pulse-width modulation can act as an efficient, fast and grid-friendly V2G resource.

Keywords Bidirectional wireless power transfer, Double-sided LCC compensation, Phase-shift modulation, Power quality, Vehicle-to-grid, Zero-voltage switching.

1. Introduction

The electrification of road transport is changing the way distribution networks are planned and operated. The charging infrastructure of the fast-growing electric car fleet is now a significant electrical load

(International Energy Agency, 2025), and in many emerging economies, including those of sub-Saharan Africa, it will be connected to grids that already suffer from limited capacity, weak feeders and poor voltage regulation, so that the interaction between charging equipment and the grid becomes a first-order concern (Pretorius et al., 2024). At the same time, the battery of a parked vehicle is a large, fast-responding and largely idle energy store. Vehicle-to-grid (V2G) operation has therefore been studied extensively since the early analyses of Kempton and Tomić (2005), which identified frequency regulation and spinning reserve as the most valuable early markets. Later reviews added reactive-power and voltage support, peak shaving, harmonic compensation and renewable-energy firming (Alamgir et al., 2025; Ravi & Aziz, 2022; Yilmaz & Krein, 2013), while highlighting costs such as additional battery degradation and the need for communication and control infrastructure (Sagaria et al., 2025; Yilmaz & Krein, 2013).

Wireless (inductive) power transfer (WPT) is an attractive way of connecting the vehicle to the grid for such services: a wireless charger needs no plug, cable or user action, so a vehicle parked over a ground pad is *always* available for scheduling, which is precisely the property that V2G aggregators value (Amjad et al., 2022; Li & Mi, 2015; Mahesh et al., 2021). SAE J2954 defines interoperable light-duty WPT power classes up to 11 kVA at 85 kHz, and ISO 15118-20 provides the communication layer for bidirectional power transfer for both conductive and wireless charging (International Organization for Standardization, 2022; SAE International, 2024). The current revision of SAE J2954, however, specifies only forward (grid-to-vehicle, G2V) power transfer and leaves bidirectional transfer to future revisions (SAE International, 2024), so the technical basis for bidirectional wireless V2G is still being established.

A bidirectional WPT charger consists of two active full bridges coupled through a loosely coupled transformer with resonant compensation networks; the double-sided LCC (DS-LCC) network is now a preferred topology for medium- and high-power vehicles and has been demonstrated in both directions up to 20 kW (Li et al., 2015; Mohammad et al., 2021; Rayan et al., 2023; Venkatesan et al., 2022). The power flow of such a dual-active-bridge (DAB)-type resonant converter is controlled by phase-shift modulation. In single-phase-shift (SPS) modulation only the phase displacement between the two bridge voltages is varied; dual-phase-shift (DPS) adds an equal inner phase shift (pulse-width reduction) to both bridges; and triple-phase-shift (TPS) varies the two inner phase shifts independently (Krismer & Kolar, 2012; Zhao et al., 2012, 2014). The extra degrees of freedom can be used to reduce circulating current, extend zero-voltage switching (ZVS) and improve light-load efficiency, as reviewed in Section 2.

Most of this literature, however, treats the WPT stage as an isolated DC-DC converter fed by an ideal DC source, and the grid-side active front end (AFE), which must synchronise to the network, regulate the DC link and deliver the actual grid services, is omitted or modelled as a constant voltage. Conversely, studies of V2G services and of single-phase grid-connected converter control usually represent the vehicle side as a controlled current or power source (Ciobotaru et al., 2006; Golestan et al., 2017; Kisacikoglu et al., 2013; Liserre et al., 2005; Teodorescu et al., 2006).

This paper addresses this gap, formulated as four research questions in Section 2.4, for a 7.7-kW (SAE J2954 WPT2 class), 85-kHz bidirectional DS-LCC wireless V2G charger connected to a 230-V, 50-Hz single-phase supply. The specific contributions are:

1) A unified analytical framework: a fundamental-frequency model of the DS-LCC link that explains why SPS control is inherently inefficient at light load, a multi-harmonic steady-state model with switching-edge ZVS and loss evaluation, and the grid-side relations for the AFE and the DC link.
2) A ZVS-constrained, loss-minimising synthesis of SPS, DPS and TPS trajectories and their comparison in both directions over 10%–100% load and a 300–400 V battery window, using 240 switching-level MATLAB/Simulink operating points cross-validated against the analytical model.
3) A switching-level grid-to-battery Simulink model with complete digital control, used to quantify power quality, power-reversal dynamics, four-quadrant P–Q capability and IEEE Std 1547-type frequency-watt and volt-var support on stiff, distorted and weak grids, including a large-signal

instability caused by the grid-voltage feed-forward on a weak feeder and its remedy.

4) An assessment, against the relevant standards, of whether a bidirectional wireless charger of this class can provide useful grid support, with the design trade-offs and limitations that govern that answer.

MATLAB/Simulink (Simscape Electrical) is used for all electrical simulations, and Python for model-based optimisation, data processing and visualisation.

2. Related Work

2.1. Bidirectional wireless power transfer and compensation

Reviews of inductive electric vehicle charging cover pad design, compensation topologies, power electronics, safety and grid impacts (Amjad et al., 2022; Li & Mi, 2015; Mahesh et al., 2021; Rayan et al., 2023). The DS-LCC network is attractive because its resonant frequency is independent of the coupling and the load and, with the tuning used in this work, the primary-coil current depends only on the primary bridge voltage (Li et al., 2015). Li et al. (2015) reported 96% DC-to-battery efficiency for a 7.7-kW prototype, and Mohammad et al. (2021) demonstrated a 20-kW bidirectional LCC–LCC system with 96.1% and 96.2% DC-DC efficiency in the G2V and V2G directions respectively. Shi et al. (2021) showed that DS-LCC systems with active rectifiers can exhibit current oscillations caused by inter-harmonics and admittance amplification, which underlines the importance of harmonic-aware modelling. Bidirectional operation and generalised steady-state models that include harmonics were developed by Madawala and Thrimawithana (2011) and Thrimawithana and Madawala (2013), and Bertoluzzo et al. (2023) designed a two-level controller for a bidirectional WPT system with vehicle-to-home functionality, including the communication delay of the wireless link. Misalignment tolerance and coupling variation have been addressed by coil and compensation design (ElGhanam et al., 2021) and by multivariable control (Liu et al., 2020).

2.2. Phase-shift modulation and soft switching

For the DAB converter, optimised TPS trajectories that minimise conduction loss, root-mean-square (RMS) current or current stress have been derived analytically (Bhattacharjee & Batarseh, 2020; Krismer & Kolar, 2012) and with learning-based methods (Tang et al., 2022; Younis et al., 2025). In resonant WPT converters the bridge currents are quasi-sinusoidal and shaped by the compensation network, so these results cannot be transferred directly. Lu et al. (2024) derived a unified optimal TPS scheme for a series-series bidirectional inductive power transfer system with full-range ZVS and minimum resonant current; Wang et al. (2025) extended TPS analysis to asymmetric parameters and showed that low-order harmonics significantly affect power and efficiency; Venkatesan et al. (2024) reported a DPS-based bidirectional controller at 3.7 kW and 85 kHz; and Zhang et al. (2022) showed that a 90° dual-side phase shift avoids hard switching in strongly coupled systems. For LCC–LCC systems, hybrid modulation (Huang et al., 2024), hybrid asymmetric-voltage-cancellation control (Peng et al., 2025), DPS with switch-controlled capacitors (Fu et al., 2023) and variable-angle phase-shift control (Jiang et al., 2021) have all been proposed to keep ZVS and high efficiency over wide load ranges. Wide-bandgap SiC devices, whose low switching losses make 85-kHz operation at kilowatt levels practical, are now the norm in such converters (Li et al., 2021; She et al., 2017; Yanagi et al., 2025).

2.3. Grid interface and V2G services

The grid side of a single-phase bidirectional charger is normally a full-bridge pulse-width modulation (PWM) converter with an L or LCL filter, controlled with proportional-resonant (PR) current controllers and selective harmonic compensation (Teodorescu et al., 2006; Zmood & Holmes, 2003), damped LCL filters (Li & Lin, 2022; Liserre et al., 2005; Upadhyay et al., 2024) and second-order generalised-integrator (SOGI) phase-locked loops (PLLs; Bamigbade et al., 2022; Ciobotaru et al., 2006; Golestan et al., 2017). The power pulsation at twice the line frequency appears as DC-link ripple, which reactive-power operation increases (Kisacikoglu et al., 2013; Zhang et al., 2020). Harmonic emission limits are set by IEEE Std 519-2022, IEEE

Std 1547-2018 and the IEC 61000-3-2/-3-12 series (IEEE, 2018, 2022; International Electrotechnical Commission, 2021, 2024); IEEE Std 1547-2018 also defines the volt-var and frequency-droop functions that a distributed energy resource may be required to provide.

2.4. Research gap

The bidirectional and phase-shift-controlled WPT studies reviewed above report DC-DC results only: 96%–96.2% efficiency at 7.7–20 kW with fixed or phase-shift control (Li et al., 2015; Mohammad et al., 2021), full or wide-range ZVS at 1.2–3.7 kW with hybrid or dual-phase-shift modulation (Huang et al., 2024; Peng et al., 2025; Venkatesan et al., 2024), and 95.1% peak efficiency at 250 W with optimal TPS (Lu et al., 2024). The grid-side converter, its power quality and grid-support functions are outside their scope. The present work combines both sides: the modulation strategies are compared not only by DC-DC efficiency but also by their effect on the grid interface, and the complete chain is evaluated against grid-support and power-quality requirements.

Several practical questions are therefore rarely answered in one consistent framework, and they define the research questions (RQ) of this study. RQ1: How do the phase-shift strategies compare in both power-flow directions once realistic losses, ZVS and battery-voltage variation are included? RQ2: Does the WPT modulation affect the power quality seen by the grid? RQ3: How fast can the complete chain reverse its power flow? RQ4: Can a wireless V2G charger deliver the grid-support functions of IEEE Std 1547-2018 while meeting the harmonic limits of IEEE Std 519-2022 and IEC 61000-3-12 (IEEE, 2018, 2022; International Electrotechnical Commission, 2021)? RQ1 is addressed in Sections 7.1 and 7.2, RQ2 in Sections 7.3 and 7.7, RQ3 in Sections 7.3 and 7.8, and RQ4 in Sections 7.4–7.7 and 8.1.

3. System Description and Converter Topology

Figure 1 shows the architecture of the bidirectional wireless V2G charger. The ground (off-board) assembly comprises a single-phase full-bridge active front end (AFE) with an LCL filter, a 400-V DC link and a high-frequency full bridge B1 that drives the primary DS-LCC network. The vehicle (on-board) assembly comprises the secondary DS-LCC network, an active full bridge B2, a DC capacitor and the traction battery. Power flows from grid to vehicle (G2V, charging) or from vehicle to grid (V2G, discharging) with the same hardware; the direction is determined only by the modulation of the two high-frequency bridges. Three controllers are used: the AFE controller on the ground side, the WPT battery-power controller, and a supervisor that receives the active- and reactive-power dispatch (for example, from an aggregator over an ISO 15118-20 link (International Organization for Standardization, 2022)) and implements the grid-support functions. Throughout this study, the communication between the supervisor and the ground-side and vehicle-side controllers is assumed to be ideal and delay-free, i.e., references and measurements are exchanged instantaneously; the effect of a finite communication delay over the wireless link is discussed in Section 8.3.

The power stage of the WPT link is shown in Figure 2. Each side consists of a compensation inductor L_{fx}, a parallel capacitor C_{fx} and a series capacitor C_x connected to the coil L_x ($x = 1$ for the ground side and $x = 2$ for the vehicle side), and the two coils are coupled through the mutual inductance $M = k\sqrt{L_1 L_2}$. The bridge AC voltages are u_1 and u_2, and i_1, i_p, i_s and i_2 denote the bridge-1 current, the primary and secondary coil currents and the current into bridge 2, respectively.

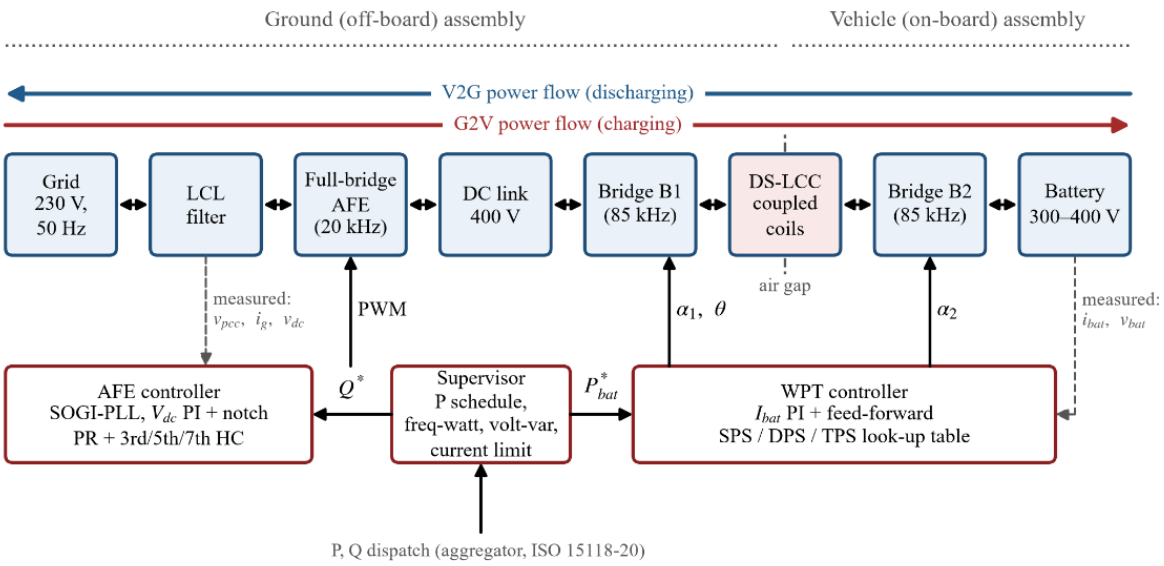


Figure 1. Architecture of the bidirectional wireless V2G charger and its control system

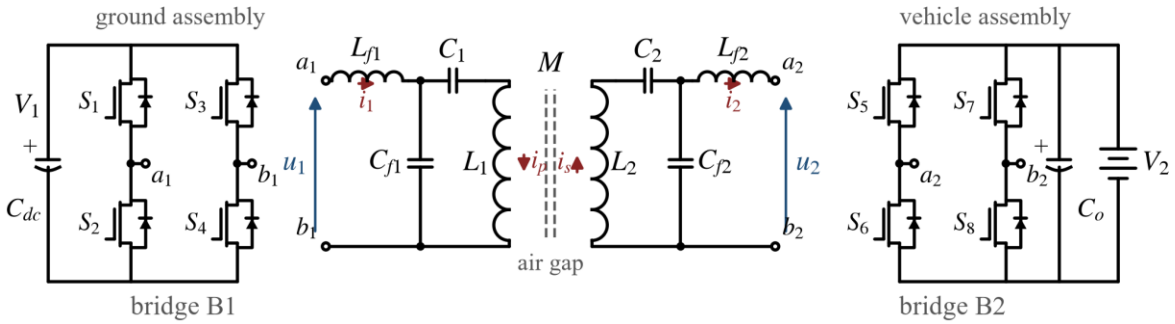


Figure 2. Power stage of the bidirectional double-sided LCC wireless power transfer link

The design specification and the resulting component values are listed in Table 1. The power level corresponds to the SAE J2954 WPT2 class (7.7 kVA) and the operating frequency to the SAE J2954 nominal frequency of 85 kHz (SAE International, 2024). The coils are assumed to be identical with $L_1 = L_2 = 120\ \mu$H and a nominal coupling coefficient of $k = 0.20$, typical of aligned light-duty vehicle pads at the nominal air gap (Li et al., 2015; Mahesh et al., 2021). The coupling is constant during each simulation and is not estimated by the controller; the effect of misalignment and air-gap variation ($k = 0.15$–0.25) on power capability, efficiency and ZVS is examined in Section 7.2. The compensation inductance $L_f = 22\ \mu$H was chosen so that the rated power is reached with margin at the lowest battery voltage and with reduced pulse widths, as explained in Section 4.2. The parasitic resistances correspond to quality factors of about 430 for the Litz-wire coils and 235 for the compensation inductors, film capacitors with a loss tangent of 5×10^{-4}, and 1200-V SiC MOSFETs with an on-state resistance of 35 mΩ (Li et al., 2021; She et al., 2017). The grid-side LCL filter is designed by the procedure of Liserre et al. (2005) for a 20-kHz unipolar PWM converter.

Table 1. Design specification and parameters of the bidirectional wireless V2G charger

Parameter	Symbol	Value
Rated battery power (SAE J2954 WPT2)	P_r	7.7 kW
Operating frequency	f_0	85 kHz
DC-link voltage	V_1	400 V
Battery voltage (nominal / range)	V_2	350 V / 300–400 V
Coil self-inductances	L_1, L_2	120 μH
Coupling coefficient (nominal)	k	0.20 ($M = 24$ μH)
Compensation inductors	L_{f1}, L_{f2}	22.0 μH
Parallel compensation capacitors	C_{f1}, C_{f2}	159.4 nF
Series compensation capacitors	C_1, C_2	35.77 nF
Coil / inductor AC resistances	R_L, R_{Lf}	0.15 Ω / 0.05 Ω
Capacitor equivalent series resistance (ESR) ($\tan\delta = 5 \times 10^{-4}$)	R_{Cf}, R_C	5.9 mΩ / 26.2 mΩ
SiC MOSFET on-state resistance	R_{on}	35 mΩ
Vehicle DC capacitor / battery resistance	C_o, R_{bat}	100 μF / 0.1 Ω
Grid voltage and frequency	V_g, f_g	230 V, 50 Hz
Grid (Thevenin) impedance, nominal	R_{grid}, L_{grid}	0.05 Ω, 0.1 mH
LCL filter	L_c, C_{fg}, L_{g2}	1.0 mH, 6.8 μF, 0.5 mH
Filter damping resistor	R_d	2.0 Ω
DC-link capacitance	C_{dc}	2.0 mF
AFE switching / sampling frequency	f_{sw}	20 kHz
AFE current limit	I_{max}	40 A rms (9.2 kVA)

4. Mathematical Modelling

4.1. Bridge voltages

Each full bridge is operated at a constant 50% duty cycle per leg. Shifting the two legs of bridge x by $\pi - \alpha_x$ produces a three-level quasi-square voltage of pulse width $\alpha_x \in (0, \pi]$, and shifting the whole of bridge 2 with respect to bridge 1 by the outer phase angle θ controls the power flow. With the time origin at the centre of the positive pulse of u_1, the Fourier series of the bridge voltages are

$$u_x(t) = \sum_{n=1,3,5,\ldots} \frac{4V_x}{n\pi} \sin\left(\frac{n\alpha_x}{2}\right) \cos[n(\omega_0 t + \delta_x)], \qquad \delta_1 = 0, \;\; \delta_2 = \theta, \tag{1}$$

where $\omega_0 = 2\pi f_0$, and the RMS value of the fundamental is

$$U_x = \frac{2\sqrt{2}}{\pi} V_x \sin\left(\frac{\alpha_x}{2}\right). \tag{2}$$

SPS modulation keeps $\alpha_1 = \alpha_2 = \pi$ and varies only θ; DPS uses $\alpha_1 = \alpha_2 = \alpha$; TPS varies α_1, α_2 and θ independently. Positive θ corresponds to G2V operation and negative θ to V2G operation with the coil polarity of Figure 2.

4.2. Fundamental-frequency model of the DS-LCC link

Both compensation networks are tuned to ω_0 according to Li et al. (2015)

$$\omega_0^2 L_{fx} C_{fx} = 1, \qquad \omega_0^2 \left(L_x - L_{fx}\right) C_x = 1, \qquad x \in \{1,2\}, \tag{3}$$

which gives the capacitor values of Table 1. Neglecting losses and harmonics and writing the fundamental phasors as $\boldsymbol{U}_1 = U_1 \angle 0$ and $\boldsymbol{U}_2 = U_2 \angle \theta$, Kirchhoff's voltage law applied to the four meshes of Figure 2 with the tuning (3) yields

$$\boldsymbol{I}_p = \frac{\boldsymbol{U}_1}{j\omega_0 L_{f1}}, \qquad \boldsymbol{I}_s = \frac{-\boldsymbol{U}_2}{j\omega_0 L_{f2}},$$
$$\boldsymbol{I}_1 = \frac{M\,\boldsymbol{U}_2}{j\omega_0 L_{f1} L_{f2}}, \qquad \boldsymbol{I}_2 = \frac{-M\,\boldsymbol{U}_1}{j\omega_0 L_{f1} L_{f2}}. \tag{4}$$

Equation (4) shows the well-known current-source behaviour of the DS-LCC network: each coil current is fixed by the bridge voltage on its own side, and each bridge current is fixed by the bridge voltage on the *opposite* side, independently of the load and of θ. The active power delivered by bridge 1, $P = \mathrm{Re}\{\boldsymbol{U}_1 \boldsymbol{I}_1^*\}$, which equals the power absorbed by bridge 2 in the lossless case, follows from (2) and (4):

$$P = \frac{M\,U_1 U_2}{\omega_0 L_{f1} L_{f2}} \sin\theta = \frac{8\,M\,V_1 V_2}{\pi^2\,\omega_0 L_{f1} L_{f2}} \sin\left(\frac{\alpha_1}{2}\right) \sin\left(\frac{\alpha_2}{2}\right) \sin\theta. \tag{5}$$

For the parameters of Table 1, the coefficient $8MV_1V_2/(\pi^2\omega_0 L_{f1} L_{f2})$ equals 10.54 kW at $V_2 = 350$ V, so that 7.7 kW requires $\sin\theta \sin(\alpha_1/2)\sin(\alpha_2/2) = 0.731$. The reactive power at the terminals of bridge 1 is

$$Q_1 = \mathrm{Im}\{\boldsymbol{U}_1 \boldsymbol{I}_1^*\} = \frac{M\,U_1 U_2}{\omega_0 L_{f1} L_{f2}} \cos\theta, \tag{6}$$

and a symmetrical expression holds for bridge 2. Thus for $0 < \theta < 90^\circ$ both bridges see an inductive (lagging) fundamental current, which is the condition for ZVS of the switching devices, while at $\theta = 90^\circ$ the fundamental reactive power is zero and soft switching relies only on the harmonic currents.

Equation (4) also explains the main weakness of SPS modulation. Because U_1 and U_2 are fixed at their maxima when $\alpha_1 = \alpha_2 = \pi$, all four currents keep their full-power magnitudes (for example, $I_p = 30.65$ A and $I_2 = 33.44$ A at $V_2 = 350$ V) regardless of the transferred power, and the power is reduced only by reducing $\sin\theta$, i.e., by increasing the circulating reactive power (6). Writing the conduction losses as $P_{cond} = R_p I_p^2 + R_s I_s^2 + R_1 I_1^2 + R_2 I_2^2$, with $R_p = R_{L1} + R_{C1}$ and $R_1 = R_{Lf1} + 2R_{on}$ (two devices conduct at any instant) and similarly for the secondary side, and substituting (4), gives

$$P_{cond} \approx a\,U_1^2 + b\,U_2^2, \qquad c = \frac{M}{\omega_0 L_{f1} L_{f2}},$$
$$a = \frac{R_p}{(\omega_0 L_{f1})^2} + R_2 c^2, \qquad b = \frac{R_s}{(\omega_0 L_{f2})^2} + R_1 c^2. \tag{7}$$

With SPS, (7) evaluates to about 529 W at any power level for the present design, which is the origin of the collapse of light-load efficiency reported in Section 7.1. Minimising (7) subject to $P = cU_1U_2\sin\theta$ gives $\theta = 90^\circ$, $U_1/U_2 = (b/a)^{1/4}$ and

$$\frac{P_{cond,\min}}{P} = \frac{2\sqrt{ab}}{c}, \tag{8}$$

which equals 4.98% for this design (a fundamental-frequency upper bound of about 95% on the link efficiency, before switching losses and harmonic currents are included). The minimum-conduction-loss trajectory therefore requires the bridge voltages to be reduced in proportion to $\sqrt{P}$, which DPS and TPS can do, while keeping θ near 90°. However, $\theta = 90^\circ$ eliminates the inductive reactive current needed for ZVS, so the true optimum is a compromise between conduction and switching losses that must be found with a model that includes harmonics and switching transitions.

4.3. Multi-harmonic steady-state model

Because the bridge voltages contain strong odd harmonics, especially when $\alpha_x < \pi$, the fundamental model is not accurate enough to predict ZVS or the switching instants. The steady state is therefore computed by superposition of the odd harmonics $n = 1,3,\ldots,199$ of (1). Bridge conduction is represented by $2R_{on}$ in series with each bridge branch. For each harmonic, the mesh currents $\boldsymbol{J}_n = [\boldsymbol{I}_{1,n}\ \boldsymbol{I}_{p,n}\ \boldsymbol{I}_{s,n}\ \boldsymbol{I}_{2,n}]^T$ satisfy

$$\begin{bmatrix} z_{f1}+z_{cf1} & -z_{cf1} & 0 & 0 \\ -z_{cf1} & z_{cf1}+z_p & jn\omega_0 M & 0 \\ 0 & jn\omega_0 M & z_s+z_{cf2} & -z_{cf2} \\ 0 & 0 & -z_{cf2} & z_{f2}+z_{cf2} \end{bmatrix} \boldsymbol{J}_n = \begin{bmatrix} \boldsymbol{U}_{1,n} \\ 0 \\ 0 \\ -\boldsymbol{U}_{2,n} \end{bmatrix}, \tag{9}$$

where $z_{fx} = R_{Lfx} + 2R_{on} + jn\omega_0 L_{fx}$, $z_{cfx} = R_{Cfx} + 1/(jn\omega_0 C_{fx})$, $z_p = R_{C1} + 1/(jn\omega_0 C_1) + R_{L1} + jn\omega_0 L_1$ and z_s is defined similarly. The DC-side powers of the two bridges, written with peak-value phasors, are

$$P_1 = \tfrac{1}{2}\textstyle\sum_n \mathrm{Re}\{\boldsymbol{U}_{1,n}\boldsymbol{I}^*_{1,n}\}, \qquad P_2 = \tfrac{1}{2}\textstyle\sum_n \mathrm{Re}\{\boldsymbol{U}_{2,n}\boldsymbol{I}^*_{2,n}\}, \tag{10}$$

and the time-domain currents are recovered as $i(t) = \sum_n \mathrm{Re}\{\boldsymbol{I}_n e^{jn\omega_0 t}\}$.

4.4. Soft-switching and loss model

At every transition of a bridge leg, the current flowing out of the leg mid-point determines whether the incoming device turns on at zero voltage. Defining i_{zvs} as the current that discharges the output capacitance of the incoming device (positive for ZVS), full ZVS requires

$$i_{zvs} \geq I_{zvs,\min} = \frac{2\,C_{oss,eq}\,V_x}{t_d}, \tag{11}$$

where $C_{oss,eq}$ is the charge-equivalent output capacitance and t_d the dead time. The factor 2 arises because, during the dead time, the leg current must discharge the output capacitance of the incoming device and, at the same time, charge that of the outgoing device of the same leg, so that it has to displace twice the charge of a single device. With $C_{oss,eq} \approx 190$ pF, $t_d = 100$ ns and $V_x = 400$ V, $I_{zvs,\min} \approx 1.5$ A. The energy dissipated in a transition is modelled with a linearised loss model representative of a 1200-V, 30–40-mΩ-class SiC MOSFET at a reference voltage $V_{ref} = 400$ V and scaled linearly with V_x:

$$E_{tr} = \frac{V_x}{V_{ref}} \begin{cases} E_{off,0} + E_{off,1}\, i_{zvs}, & i_{zvs} \geq I_{zvs,\min} \\ E_{oss}\left(1 - \dfrac{i_{zvs}}{I_{zvs,\min}}\right) + E_{off,0} + E_{off,1}\, i_{zvs}, & 0 \leq i_{zvs} < I_{zvs,\min} \\ E_{on,0} + E_{on,1}\,|i_{zvs}|, & i_{zvs} < 0 \end{cases} \tag{12}$$

The three cases correspond to full ZVS, partial ZVS and hard switching, respectively, with $E_{off,0} = 3\ \mu$J, $E_{off,1} = 2\ \mu$J/A, $E_{oss} = 20\ \mu$J, $E_{on,0} = 20\ \mu$J and $E_{on,1} = 7\ \mu$J/A. The switching loss of bridge x is $P_{sw,x} = f_0 \sum E_{tr}$ over its four transitions per period. Because the hard-switching energies of real devices depend strongly on the gate drive and layout, the sensitivity of the conclusions to these values is examined explicitly in Section 7.2. The model further assumes a temperature-independent on-state resistance, neglects the diode conduction during the 100-ns dead time (1.7% of the period) and the gate-drive losses, and assumes that the energy stored in C_{oss} is recovered under full ZVS; the AFE devices use the same energy model with hard switching at every edge. The conduction loss P_{cond} is obtained from the RMS currents in all resistive elements, and the link efficiency is

$$\eta_{dc} = \frac{P_{out}}{P_{out} + P_{cond} + P_{sw,1} + P_{sw,2}}, \tag{13}$$

where P_{out} is the power delivered to the battery in G2V operation and to the DC link in V2G operation.

4.5. Grid-side model

The AFE is connected to the point of common coupling (PCC) through an LCL filter with a damping resistor R_d in series with C_{fg}. With the grid treated as a short circuit at frequencies above the fundamental, the transfer function from the converter voltage to the grid current is

$$G_{LCL}(s) = \frac{R_d C_{fg} s + 1}{L_c L_g C_{fg} s^3 + (L_c + L_g) R_d C_{fg} s^2 + (L_c + L_g) s}, \qquad L_g = L_{g2} + L_{grid}, \tag{14}$$

which has its resonance at $f_{res} = \frac{1}{2\pi}\sqrt{(L_c + L_g)/(L_c L_g C_{fg})} = 3.15$ kHz for the nominal grid, i.e., between ten times the line frequency and one-half of the switching frequency, as recommended by Liserre et al. (2005).

With $v_{pcc} = \sqrt{2} V \cos\omega_g t$ and $i_g = \sqrt{2} I \cos(\omega_g t - \varphi)$, the instantaneous single-phase power is

$$p_g(t) = VI\cos\varphi + VI\cos(2\omega_g t - \varphi), \tag{15}$$

so the DC link must buffer a pulsation of amplitude $S = VI$ at twice the line frequency, regardless of the power factor. Since the WPT stage draws an almost constant power, the energy balance $C_{dc} V_{dc}\, \mathrm{d}\tilde{v}_{dc}/\mathrm{d}t = S\cos(2\omega_g t - \varphi)$ gives the peak-to-peak DC-link ripple

$$\Delta V_{dc,pp} = \frac{S}{\omega_g C_{dc} V_{dc}}, \tag{16}$$

which equals 33.2 V (8.3%) for $S = 8.35$ kVA, the grid-side apparent power at rated G2V operation. Equation (16) also shows that reactive-power support increases the DC-link ripple through S, consistent with Kisacikoglu et al. (2013). The same small-signal energy balance gives the plant used for the DC-link voltage controller, $\tilde{v}_{dc}(s)/\tilde{p}(s) = 1/(sC_{dc}V_{dc})$.

5. Converter Control and Optimisation

Figure 3 details the three control layers. All controllers are discrete and are executed once per AFE switching period ($T_c = 50$ μs), with the measurements sampled synchronously with the PWM carrier after first-order 2-kHz anti-aliasing filters; the high-frequency bridges are modulated at 85 kHz by a phase-shift modulator that receives $(\alpha_1, \alpha_2, \theta)$ from the WPT controller. Discrete coefficients are obtained with the Tustin transformation, pre-warped at the frequency of interest. The controller parameters are given with each controller below.

5.1. Modulation strategies and their synthesis

For a given battery-power reference P^* and voltages V_1, V_2, the operating point $(\alpha_1, \alpha_2, \theta)$ of each strategy is computed off-line with the multi-harmonic model of Section 4, following the procedure of Figure 4. For any candidate pulse widths, the outer phase shift is obtained from the power equation

$$P_{bat}(\alpha_1, \alpha_2, \theta) = P_2(\alpha_1, \alpha_2, \theta) - P_{sw,2}(\alpha_1, \alpha_2, \theta) = P^* \tag{17}$$

by bracketing and Brent's method, and the root with the lower total loss is retained. The strategies compared in this paper are:

- SPS: $\alpha_1 = \alpha_2 = \pi$; θ from (17). One degree of freedom.
- DPS (minimum loss): $\alpha_1 = \alpha_2 = \alpha$, with α chosen to minimise $P_{loss} = P_{cond} + P_{sw,1} + P_{sw,2}$. Two degrees of freedom and no explicit soft-switching requirement, so the optimiser may accept hard switching if this lowers the total loss.
- TPS (ZVS-constrained): α_1 and α_2 independent, chosen to minimise

$$J = P_{loss} + \lambda \max\left(0,\ I_{req} - \min_{edges} i_{zvs}\right), \tag{18}$$

with $I_{req} = I_{zvs,\min} + 0.5\ \mathrm{A} = 2$ A and $\lambda = 200$ W/A, so that all eight devices switch at zero voltage with margin whenever this is attainable. The 0.5-A margin covers model inaccuracy and look-up table (LUT) interpolation. The penalty acts as an exact penalty above a threshold. Re-optimising representative points

(10%, 50% and 100% load in both directions) gave identical trajectories, efficiencies and the full 2.0-A margin for each tested λ of 10, 20, 50, 200 and 1000 W/A, because the constraint is then active at the optimum. At $\lambda = 5$ W/A the optimiser trades the 0.5-A margin for up to 0.3 point of efficiency, and at $\lambda = 2$ W/A it accepts hard switching at 50% load. The chosen $\lambda = 200$ W/A is therefore 20 times above this threshold. Three degrees of freedom.

– DPS (ZVS-constrained), used as a reference to separate the effect of the third degree of freedom from that of the ZVS constraint: $\alpha_1 = \alpha_2$ with the cost (18).

The two-dimensional searches start from a coarse grid of (α_1, α_2) and are refined by the Nelder–Mead simplex method from the four best seeds. For closed-loop control, LUTs of $(\alpha_1, \alpha_2, \theta)$ are computed at 73 power levels, 250 W apart, between -9 kW and $+9$ kW for the nominal voltages ($V_1 = 400$ V, $V_2 = 350$ V) and coupling ($k = 0.20$), using continuation in P^* so that the trajectories are smooth. The three angles are interpolated linearly in power; the effect of interpolation and of operation away from the nominal battery voltage and coupling is quantified in Section 7.2.

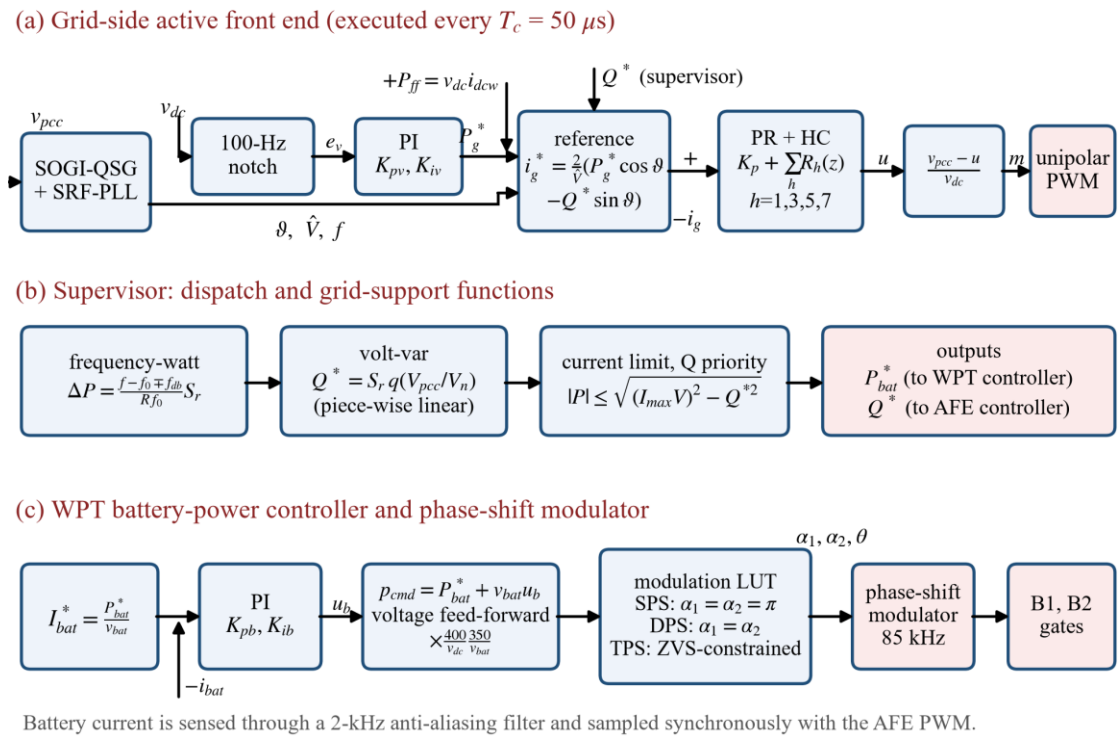


Figure 3. Control system: (a) grid-side active front end; (b) supervisor with grid-support functions; (c) WPT battery-power controller and phase-shift modulator

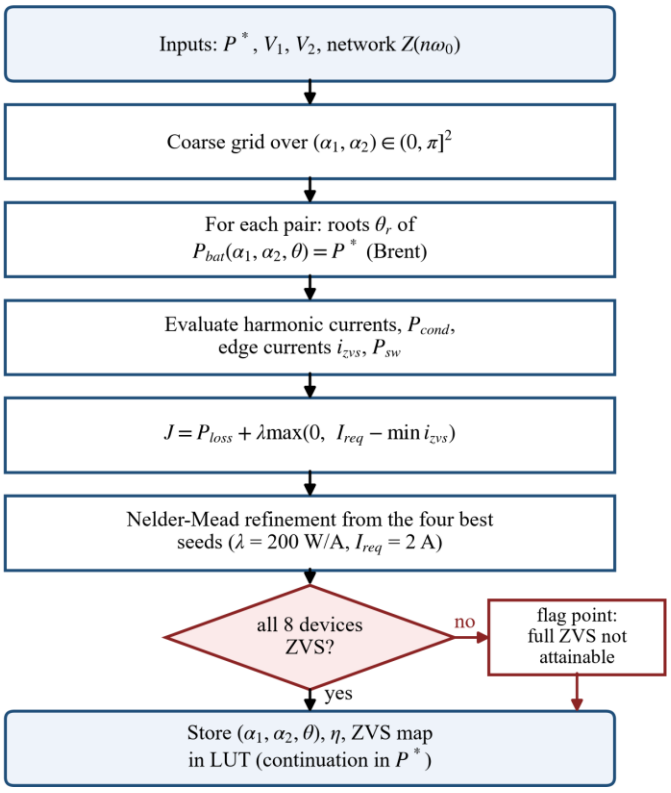


Figure 4. Flowchart of the model-based synthesis of the modulation trajectories

5.2. WPT battery-power controller

Because the DS-LCC link behaves as a current source, the battery current responds to $(\alpha_1, \alpha_2, \theta)$ within a few tens of microseconds and the battery-power loop can be designed as a simple proportional-integral (PI) controller around a feed-forward LUT:

$$p_{cmd} = P^*_{bat} + v_{bat}\left(K_{pb}\, e_b + K_{ib} \int e_b \, \mathrm{d}t\right), \qquad e_b = \frac{P^*_{bat}}{v_{bat}} - i_{bat}, \tag{19}$$

$$P_{LUT} = p_{cmd}\, \frac{400\ \mathrm{V}}{v_{dc}}\, \frac{350\ \mathrm{V}}{v_{bat}}, \qquad (\alpha_1, \alpha_2, \theta) = \mathrm{LUT}(P_{LUT}). \tag{20}$$

The voltage scaling in (20) follows from (5), in which the power is proportional to $V_1 V_2$ for given angles; it compensates the 100-Hz DC-link ripple and the battery-voltage variation in feed-forward, and the PI term removes the residual error caused by losses and LUT interpolation. The gains are $K_{pb} = 0.30$ and $K_{ib} = 754\ \mathrm{s}^{-1}$, and the integrator is clamped to ± 6 A. In a practical charger the WPT controller would run on the ground side with i_{bat} and v_{bat} transmitted over the wireless communication link, or be split between the two sides; the communication delay is not modelled here.

5.3. Active front-end control

Synchronisation. A SOGI quadrature-signal generator (Ciobotaru et al., 2006)

$$D(s) = \frac{v_\alpha}{v_{pcc}} = \frac{k\,\omega_g\, s}{s^2 + k\,\omega_g\, s + \omega_g^2}, \qquad Q(s) = \frac{v_\beta}{v_{pcc}} = \frac{k\,\omega_g^2}{s^2 + k\,\omega_g\, s + \omega_g^2}, \tag{21}$$

with $k = \sqrt{2}$, feeds a synchronous-reference-frame PLL whose PI regulator acts on the normalised quadrature voltage $\varepsilon = v_q/(\sqrt{2}V_g)$, $\hat{\omega} = \omega_g + K_{p,pll}\varepsilon + K_{i,pll}\int \varepsilon \, \mathrm{d}t$, with $K_{p,pll} = 2\zeta\omega_n$ and $K_{i,pll} = \omega_n^2$ for $\omega_n = 2\pi \cdot 20$ rad/s and $\zeta = 0.707$. The PLL provides the phase ϑ, the peak voltage $\hat{V}$, the frequency $\hat{f}$ and a 5-Hz filtered RMS voltage for the volt-var function.

DC-link voltage control. With the plant $1/(sC_{dc}V_{dc})$ derived in Section 4, a PI controller with $K_{pv} = 2\pi f_{cv} C_{dc} V_{dc}$ and $K_{iv} = K_{pv}\, 2\pi f_{cv}/5$ with $f_{cv} = 15$ Hz gives a crossover frequency of 15.1 Hz ($K_{pv} = 75.4$ W/V, $K_{iv} = 1421$ W/(V·s), integrator limited to ± 3 kW) and a phase margin of 69°, including the phase lag of the notch filter, the anti-aliasing filter and the 1.5-sample delay. A 100-Hz notch filter ($Q = 1$) removes the ripple (16) from the feedback so that it does not distort the current reference. The measured DC power of the WPT stage, $P_{ff} = v_{dc}\, i_{dcw}$, is added as a feed-forward term, so that the DC-link controller only has to correct the losses and the transients:

$$P_g^* = K_{pv}\, e_v + K_{iv}\int e_v \, \mathrm{d}t + P_{ff}, \qquad e_v = V_{dc}^* - \mathrm{notch}(v_{dc}). \tag{22}$$

Current reference and current control. With i_g defined as the current drawn from the grid, $P_g^* > 0$ denoting power absorbed from the grid (charging) and $Q^* > 0$ denoting reactive power injected into the grid (capacitive operation, which raises the PCC voltage), the grid-current reference is

$$i_g^* = \frac{2}{\hat{V}}\left(P_g^* \cos\vartheta - Q^* \sin\vartheta\right), \tag{23}$$

and the current is regulated by a PR controller with resonant compensators at the 3rd, 5th and 7th harmonics (Teodorescu et al., 2006; Zmood & Holmes, 2003):

$$G_c(s) = K_p + \sum_{h\in\{1,3,5,7\}} \frac{2K_{r,h}\,\omega_c\,(s\cos\phi_h - h\omega_g \sin\phi_h)}{s^2 + 2\omega_c s + (h\omega_g)^2}, \qquad \phi_h = 1.5\, h\, \omega_g T_c, \tag{24}$$

where ϕ_h compensates the 1.5-sample computation and PWM delay at each resonant frequency, $K_{r,h} = 300$, 60, 45 and 35 V/A for $h = 1$, 3, 5 and 7, and $\omega_c = 5$ rad/s. The converter voltage reference $v_{ff} - u$, where v_{ff} is a grid-voltage feed-forward term discussed below, is normalised by the measured DC-link voltage and applied by unipolar PWM. With $K_p = 8$ V/A, the open-loop gain of the sampled loop (including the zero-order hold, one sample of computation delay and the LCL plant (14)) crosses 0 dB at about 0.86 kHz with a phase margin above 90°, and the passive damping keeps all closed-loop poles inside the unit circle (largest magnitude 0.9988) for grid inductances from 0 to 2 mH, i.e., from a stiff grid to a weak rural feeder. This small-signal result does not, however, cover the large-signal behaviour on a weak grid, where the PCC voltage itself contains the response of the filter to the converter current. Two feed-forward options are therefore provided for the term v_{ff} in the converter voltage reference $v_{ff} - u$: the anti-aliased measured PCC voltage (the default, which offers the best rejection of grid-voltage disturbances) and the in-phase output v_α of the SOGI (21), i.e., only the fundamental of the PCC voltage. Their behaviour on a weak feeder is compared in Section 7.6.

5.4. Supervisor and grid-support functions

The supervisor converts the dispatch into the battery-power and reactive-power references. Two grid-support functions of IEEE Std 1547-2018 (IEEE, 2018) are implemented with the default settings of the standard. Implementing and simulating these functions does not establish conformance with IEEE Std 1547-2018, which also covers, for example, ride-through, protection, interoperability and type testing; these aspects are outside the scope of this study. The frequency-watt (frequency-droop) function modifies the scheduled battery power P_{sch} as

$$P_{bat}^{*} = P_{sch} + \frac{\Delta f_e}{R\, f_0} S_r, \qquad \Delta f_e = \begin{cases} \hat{f} - f_0 - f_{db}, & \hat{f} - f_0 > f_{db} \\ \hat{f} - f_0 + f_{db}, & \hat{f} - f_0 < -f_{db} \\ 0, & \text{otherwise} \end{cases} \tag{25}$$

with a dead band $f_{db} = 0.036$ Hz (the IEEE Std 1547-2018 default), a droop $R = 3\%$ (more aggressive than the 5% default, chosen to exercise the full power range) and $S_r = 7.7$ kVA; $\hat{f}$ is filtered with a 10-Hz low-pass filter. An under-frequency event therefore reduces charging and, if deep enough, reverses the power flow to V2G. The volt-var function uses the IEEE Std 1547-2018 Category B default characteristic, with breakpoints at 0.92, 0.98, 1.02 and 1.08 p.u. and reactive-power limits of ± 0.44 p.u. of S_r (injection at low voltage, absorption at high voltage). Finally, the references are limited by the AFE current rating with reactive-power priority:

$$|Q^{*}| \le I_{max} V_{pcc,rms}, \qquad |P_{bat}^{*}| \le 0.9 \sqrt{(I_{max} V_{pcc,rms})^2 - Q^{*2}}, \tag{26}$$

where the factor 0.9 leaves headroom for the conversion losses between the battery and the grid, and the RMS PCC voltage in (26) is obtained from the PLL amplitude estimate as $V_{pcc,rms} = \frac{\hat{V}}{\sqrt{2}}$.

6. Simulation Methodology and Model Validation

All electrical simulations are carried out in MATLAB/Simulink R2024b with Simscape Electrical (Specialized Power Systems), and the models are built programmatically from MATLAB scripts. These scripts, the Python analysis scripts and the simulation data are available as stated in the Data Availability section.

Figure 5 shows the simulation framework and the two models developed for this study. The design specification of Table 1 and the multi-harmonic model of Section 4.3 are used to synthesise the SPS, DPS and TPS look-up tables with the procedure of Figure 4. Two switching-level Simulink models are then built. Model A contains only the WPT stage between stiff DC sources; it is used to compare the modulation strategies and to cross-validate the analytical model (Section 6.1). Model B represents the complete grid-to-battery chain together with the digital control of Section 5 and is used for all grid-interface and grid-support studies (Sections 7.3–7.8). The waveforms logged from both models are post-processed in Python to obtain the switching losses, the power-quality indices and the efficiencies. The two models and the post-processing are described below.

WPT-stage model. The first model (Model A) contains the two full bridges (MOSFET/diode universal bridges with $R_{on} = 35$ mΩ), the complete DS-LCC network with all parasitic resistances, a two-winding mutual-inductance block for the coils and stiff DC sources for V_1 and V_2. It is solved with the discrete Tustin/backward-Euler method at a fixed step of 20 ns (588 steps per switching period). Each operating point is simulated for 6 ms (more than five times the slowest envelope time constant), and the last ten switching periods are analysed. The SPS, DPS (minimum-loss), DPS (ZVS-constrained) and TPS operating points were simulated at ten power levels in each direction (10%–100% of 7.7 kW) and at $V_2 = 300$, 350 and 400 V, giving 240 operating points.

Full grid-to-battery model. The second model (Model B) adds the programmable single-phase grid (with Thevenin impedance and optional background harmonics), the LCL filter, the full-bridge AFE, the DC-link capacitor, the vehicle DC capacitor and a battery represented by an electromotive force (EMF) of 350 V behind 0.1 Ω, together with the complete digital control of Section 5. Because the 85-kHz bridges and the 50-Hz grid must be represented simultaneously, the model is solved at a fixed step of 40 ns, and signals are logged every 10 μs. Steady-state quantities are evaluated over the last ten fundamental cycles before each set-point change, i.e., at least 100 ms after the preceding transient (the grid power settles within 22 ms, Section 7.3). The nominal grid impedance ($0.05 + \mathrm{j}0.031$ Ω) corresponds to a short-circuit current of about

3.9 kA, i.e., $I_{sc}/I_L \approx 116$. Twelve scenarios were simulated: a dispatch profile (G2V 7.7 kW → V2G 7.7 kW → V2G 1.54 kW → G2V 1.54 kW) with each of the SPS, DPS and TPS look-up tables; four-quadrant P–Q operation; a frequency-watt test with under- and over-frequency events; G2V and V2G operation on a weak feeder ($R_{grid} = 0.4\ \Omega$, $L_{grid} = 1.2$ mH, $X/R = 0.94$, short-circuit ratio 12.5 with respect to 7.7 kVA) with and without volt-var, each with both grid-voltage feed-forward options; operation with a distorted grid voltage (3% 3rd, 4% 5th and 2.5% 7th harmonic, total harmonic distortion THD_v = 5.6%) with and without harmonic compensation; and a power reversal without DC-link power feed-forward.

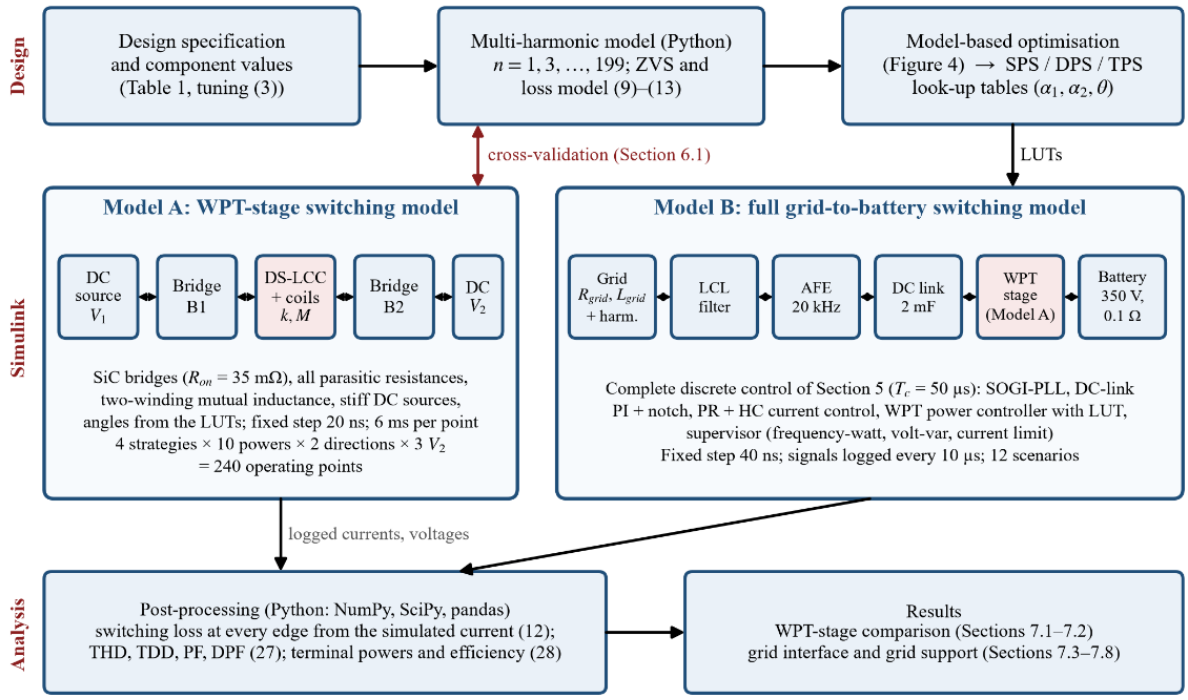


Figure 5. Simulation framework: design tools, the two switching-level MATLAB/Simulink models (Model A: WPT stage; Model B: complete grid-to-battery system with digital control) and the post-processing chain

Post-processing. The logged data are processed in Python (NumPy, SciPy, pandas and Matplotlib). In the switching-level models the devices switch instantaneously, so the simulated powers contain all conduction losses but no switching losses; the switching loss of every device is evaluated from the simulated current at each switching edge with (12) (for the AFE, hard switching at 20 kHz with the E_{on}/E_{off} terms). The grid-side quantities are evaluated over ten fundamental cycles (200 ms), as in IEC 61000-4-7, and the following metrics are used (TDD: total demand distortion; PF: power factor: DPF: displacement power factor):

$$\mathrm{THD}_I = \frac{\sqrt{\sum_{h=2}^{50} I_h^2}}{I_1}, \qquad \mathrm{TDD} = \frac{\sqrt{\sum_{h=2}^{50} I_h^2}}{I_L}, \qquad \mathrm{PF} = \frac{P}{V_{rms} I_{rms}}, \qquad \mathrm{DPF} = \cos\varphi_1, \tag{27}$$

where $I_L = 7.7\ \mathrm{kW}/230\ \mathrm{V} = 33.5$ A is the rated current used as the demand-current base, and φ_1 is the angle between the fundamental voltage and current. The grid power P_{grid} is measured at the PCC (the grid impedance is excluded), $P_{dc,WPT}$ at the DC input of bridge B1 and P_{bat} at the battery terminals, all averaged over the evaluation window. Booking each switching loss where it occurs gives the terminal powers

$$P_{in} = \begin{cases} P_{grid} + P_{sw,AFE} + P_{sw,1} & \text{(G2V)} \\ |P_{bat}| + P_{sw,2} & \text{(V2G)} \end{cases}, \qquad P_{out} = \begin{cases} P_{bat} - P_{sw,2} & \text{(G2V)} \\ |P_{grid}| - P_{sw,AFE} - P_{sw,1} & \text{(V2G)} \end{cases}, \tag{28}$$

and the grid-to-battery efficiency $\eta_{sys} = P_{out}/P_{in}$; the WPT-stage efficiency (13) is defined in the same way between the DC link and the battery.

6.1. Cross-validation of the analytical model

Figure 6 compares the multi-harmonic model with the switching-level Simulink model, which is used here as the reference; both are simulation models, so this comparison verifies the analytical model against an independent circuit simulation but does not replace experimental validation. For each operating point the model is evaluated at the same angles and voltages as the simulation, and the power error is defined as $e_P = (P_{2,model} - P_{2,sim})/|P_{2,sim}|$, where P_2 is the DC power at bridge 2 averaged over the last ten switching periods. The predicted bridge currents are practically indistinguishable from the simulated ones (panel (a)), including the sharp changes of slope caused by the three-level bridge voltages. Over all 240 operating points (panels (b)–(d)), the mean of $|e_P|$ is 0.26% and its maximum 3.5%, reached at the lightest SPS point (V2G, 10% load, $V_2 = 300$ V), where the transferred power is a small difference of large circulating powers; for $|P| \geq 1.5$ kW the maximum is 1.6%, and for DPS and TPS 0.6%. The primary-coil RMS current agrees to within 0.05% on average (0.36% maximum) and the efficiency to within 0.06 points on average (0.07 points maximum for DPS and TPS, 2.8 points at the lightest SPS point). The fundamental-frequency results are also confirmed: with SPS the simulated primary-coil current is 30.4–30.9 A at every power level, against 30.65 A from (4), and the light-load conduction loss (about 540 W) is within 2% of the 529 W of (7). All performance figures below are taken from the switching-level simulations.

7. Results

7.1. Comparison of the modulation strategies

Typical steady-state waveforms at rated and at 20% power are shown in Figure 7. At 7.7 kW, all three strategies operate with moderate phase shifts and quasi-sinusoidal currents of similar amplitude. At 1.54 kW the difference is striking: with SPS the outer phase shift falls to 10°, the two bridge voltages are almost in phase and the bridge currents remain at about 50 A peak, so that most of the current is circulating reactive current; DPS and TPS reduce the pulse widths to 47° and 55–58° respectively, and the currents fall by roughly a factor of three. The DPS (minimum-loss) trajectory keeps θ close to 76–77°, which is near the minimum-conduction-loss condition derived from (8), but at this phase shift one leg of each bridge commutates with the current in the wrong direction and is hard-switched. The ZVS-constrained TPS trajectory uses a smaller outer phase shift (43°–66°), which, according to the model, provides the inductive current needed for full ZVS of all devices.

Figure 8 presents the DC-DC efficiency of the four strategies over the whole operating range, and Table 2 summarises the results at the nominal battery voltage. The behaviour is nearly symmetrical in the two power-flow directions, which confirms that the bidirectional DS-LCC link with phase-shift control is equally suitable for V2G and for charging. SPS reaches 92.9% (G2V) and 92.3% (V2G) at rated power but degrades rapidly below about 60% load, down to 56.9% (G2V) and 20.9% (V2G) at 10% load; its average efficiency over 10%–100% load is only 83.4% (G2V) and 77.0% (V2G). As shown in Figure 9, the total loss of SPS is almost constant at about 600 W, of which more than 85% is conduction loss caused by the load-independent currents. DPS and TPS reduce the light-load loss by a factor of seven to nine (from 603 W to 70–84 W at 10% load) and keep the efficiency above 89% at 10% load and above 92.5% from 50% load upwards. The worst-case efficiency over all three battery voltages is 9.6% for SPS (V2G, 10% load, $V_2 = 400$ V), 90.7% for DPS and 89.8% for TPS.

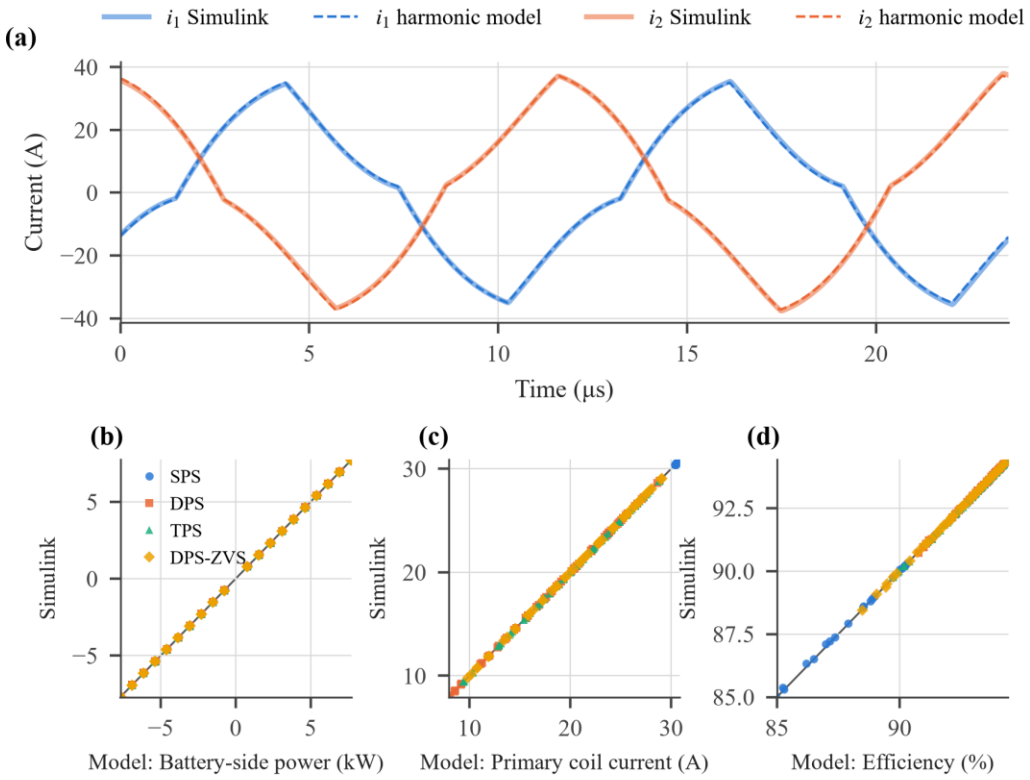


Figure 6. Cross-validation of the multi-harmonic model against the switching-level Simulink model: (a) bridge currents for TPS at 3.85 kW (G2V, $V_2 = 350$ V); (b) battery-side power, (c) primary-coil current and (d) efficiency for all 240 operating points

Table 2. Simulated WPT-stage performance at $V_2 = 350$ V (switching-level model). $\bar{\eta}$: mean over 10%–100% load; ZVS: edges with $i_{zvs} \geq 1.5$ A; hard: edges with $i_{zvs} < 0$; I_p: primary-coil RMS current

Strategy	Mode	$\eta_{10\%}$ (%)	$\eta_{50\%}$ (%)	$\eta_{100\%}$ (%)	$\bar{\eta}$ (%)	$P_{loss,100\%}$ (W)	$I_{p,10\%}$ (A)	ZVS (%)	hard (%)
SPS	G2V	56.9	86.5	92.9	83.4	591	30.6	100	0
	V2G	20.9	84.4	92.3	77.0	593	30.7	100	0
DPS (min. loss)	G2V	91.2	93.5	94.3	93.4	463	8.6	50	50
	V2G	91.0	93.4	94.2	93.2	445	8.5	50	50
DPS (ZVS)	G2V	89.9	92.9	94.3	92.8	469	10.8	94	0
	V2G	89.1	92.6	94.1	92.4	456	10.7	100	0
TPS (ZVS)	G2V	90.2	92.9	94.2	92.8	470	10.3	88	0
	V2G	90.0	92.9	94.1	92.7	452	9.5	90	0

Among the variable-pulse-width strategies, DPS (minimum loss) gives the highest efficiency in this comparison, by 0.4–0.6 points on average and by up to 1.0 point at light load, but it does so by accepting hard switching on half of the switching edges, on both bridges (Figure 10(b) and Table 3). In absolute terms this advantage is small with nominal device data: about 7 W at rated power and 9 W at 10% load in the WPT stage (Table 2), and 0.1 point at 7.7 kW and 1.0–1.1 points at 1.54 kW at system level (Table 4). Both strategies use the same three-entry look-up table and the same two independently modulated bridges, so TPS adds no hardware or real-time complexity; its cost is the off-line two-dimensional optimisation. Table 3 lists the smallest ZVS current found at any switching edge in the switching-level simulations. No TPS edge is hard-switched at any operating point of the three battery voltages: 84%–99% of the edges satisfy the full ZVS condition (11), and the remainder switch with partial ZVS down to $i_{zvs} = 0.46$ A (G2V, rated power). The model predicts the 2.0-A design value at the critical edges of both bridges, so the simulated edge currents

are up to 1.5 A lower; the edge current is a small difference of large instantaneous currents and is sensitive to the higher-order harmonics, which makes it the least accurate quantity of the harmonic model. A larger design margin, or a closed-loop dead-time adjustment, would therefore be advisable in hardware.

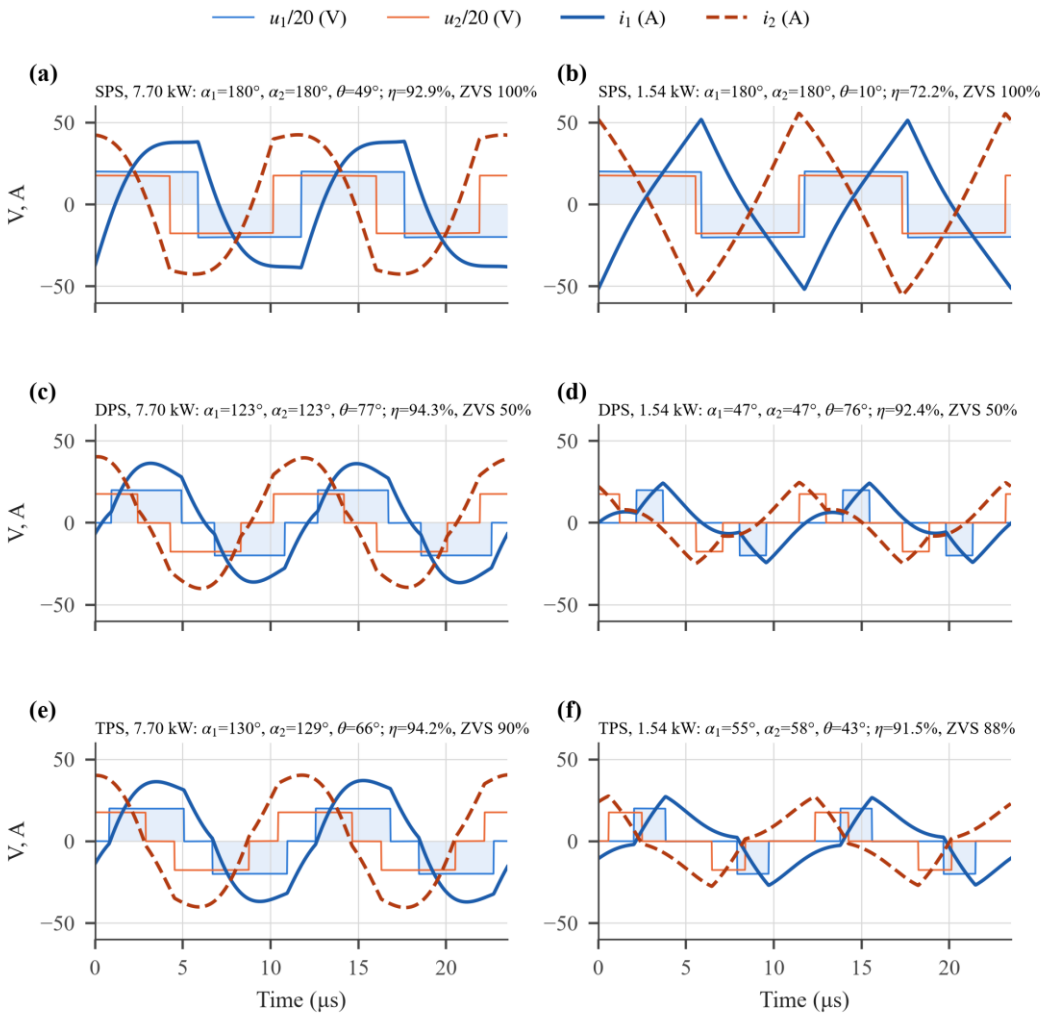


Figure 7. Simulated bridge voltages and currents (G2V, $V_2 = 350$ V) at 7.7 kW (left) and 1.54 kW (right) for (a), (b) SPS; (c), (d) DPS (minimum loss); and (e), (f) TPS (ZVS-constrained)

Constraining DPS to ZVS costs more efficiency than constraining TPS: TPS is better than ZVS-constrained DPS by 0.39, 0.18 and 0.10 points on average at $V_2 = 300$, 350 and 400 V, respectively, and by up to 1.7 points at light load at 300 V. The benefit of the third degree of freedom therefore grows with the mismatch between the DC voltages, because independent pulse widths allow the two fundamental voltages to be matched to the condition $U_1/U_2 = (b/a)^{1/4}$ of (8) while ZVS is maintained. Figure 10(a) shows that the primary-coil current of TPS falls from 27.5 A at rated power to 10.3 A at 10% load, compared with an almost constant 30.4–30.9 A for SPS, which also reduces the magnetic field emitted by the pads at partial load.

Table 3. Minimum ZVS current i_{zvs} (A) at any switching edge (switching-level simulations, worst case over $V_2 = 300$–400 V; full ZVS for $i_{zvs} \geq 1.5$ A, hard switching for $i_{zvs} < 0$) and maximum share of hard-switched edges

Strategy	Mode	10% load	50% load	100% load	10%–100%	Hard (%)
SPS	G2V	45.15	41.98	27.55	27.55	0
	V2G	45.18	42.02	28.96	28.96	0
DPS (min. loss)	G2V	−7.13	−14.89	−11.60	−14.89	51
	V2G	−6.78	−14.85	−12.58	−15.14	50
DPS (ZVS)	G2V	1.17	0.95	1.05	0.30	0
	V2G	1.76	1.58	1.28	1.28	0
TPS (ZVS)	G2V	1.08	0.83	0.46	0.46	0
	V2G	1.12	0.87	0.85	0.69	0

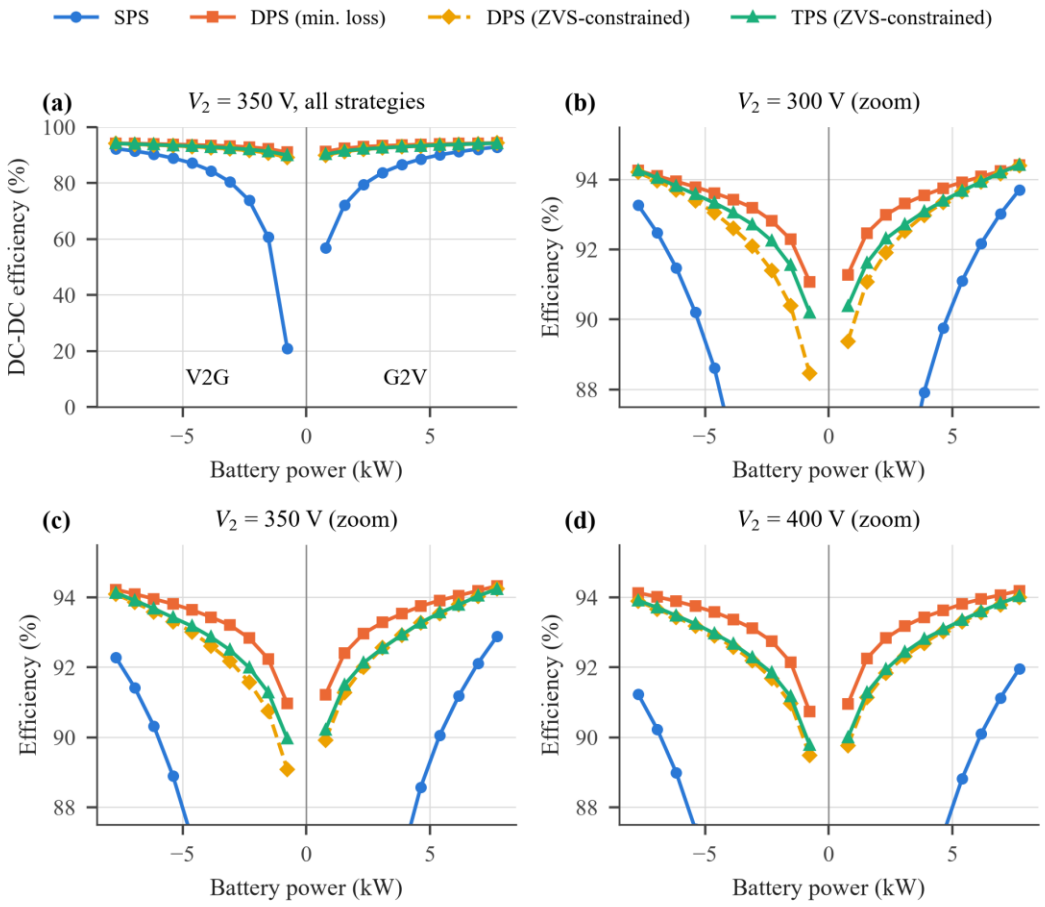


Figure 8. Simulated DC-DC efficiency of the WPT link versus battery power (negative: V2G) for the four modulation strategies: (a) full scale at $V_2 = 350$ V; (b)–(d) detail at $V_2 = 300$, 350 and 400 V

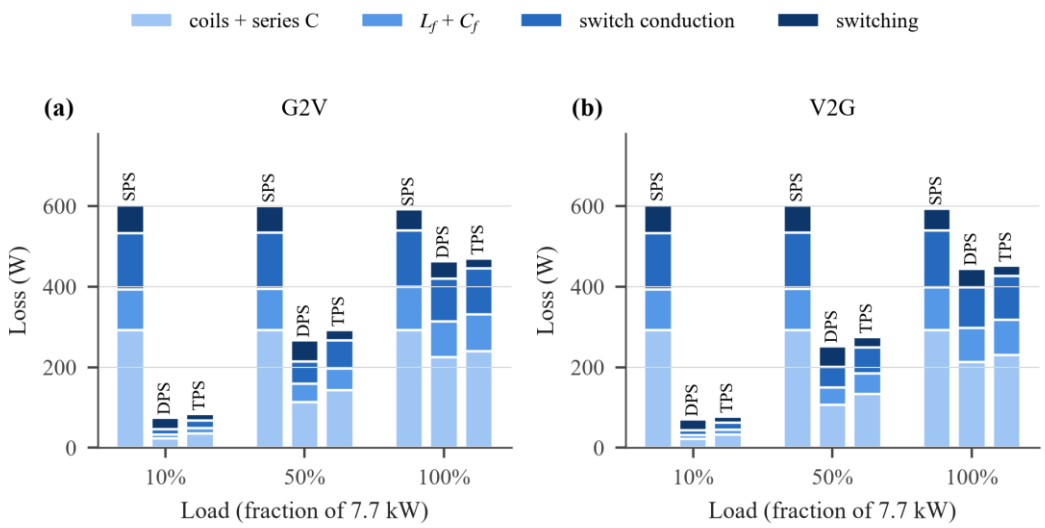


Figure 9. Loss breakdown of the WPT link at 10%, 50% and 100% of rated power ($V_2 = 350$ V) for SPS, DPS (minimum loss) and TPS: (a) G2V; (b) V2G

The component stresses are similar for the three strategies; over the complete operating range the peak voltages reach 2.31 kV across C_1 and 2.62 kV across the primary coil, which must be considered in the capacitor selection and pad insulation.

7.2. Sensitivity to the switching-loss model and to coupling variation

The ranking of DPS (minimum loss) and TPS (ZVS-constrained) depends on the hard-switching energy assumed in (12), which varies widely between devices, gate drivers and layouts. Figure 11 shows the efficiency difference between the two strategies, recalculated from the same switching-level waveforms, when the hard-switching energies ($E_{on,0}$, $E_{on,1}$ and E_{oss}) are scaled by a factor k_E. TPS becomes more efficient than DPS when k_E exceeds 1.3–1.8, depending on the load and the direction of power flow, and its advantage reaches 0.7–4.2 points at $k_E = 4$. Hard switching at 85 kHz also causes high $\mathrm{d}v/\mathrm{d}t$ and reverse-recovery stress, which the energy model does not capture. Within the device-loss range considered, ZVS-constrained TPS is therefore the less sensitive choice, and it is used for the full-system studies unless otherwise stated.

Coil misalignment and air-gap variation change the coupling coefficient, which, according to (5), scales the transferable power in proportion to M. Figure 12 shows the efficiency of re-optimised SPS, DPS and TPS trajectories for k between 0.15 and 0.25 (calculated with the cross-validated harmonic model), and the maximum lossless power with full pulse widths. For $k \geq 0.175$, the efficiency of DPS and TPS changes by less than 1 point across the whole range, because the pulse widths are simply re-adjusted to the new coupling; when its trajectories are re-optimised for each coupling, TPS meets the full-ZVS condition on all eight devices in the model. SPS, in contrast, loses efficiency as the coupling increases, because a stronger coupling forces a smaller θ for the same power and therefore more circulating current: at 20% load its efficiency falls from 76.0% to 67.2% (G2V) and from 68.4% to 51.2% (V2G) between $k = 0.15$ and $k = 0.25$. At $k = 0.15$ the maximum lossless power falls to 7.71 kW, so that rated G2V power can no longer be delivered once the losses are included; this defines the lower coupling limit of the design; below about $k = 0.16$ the battery-power reference should be derated.

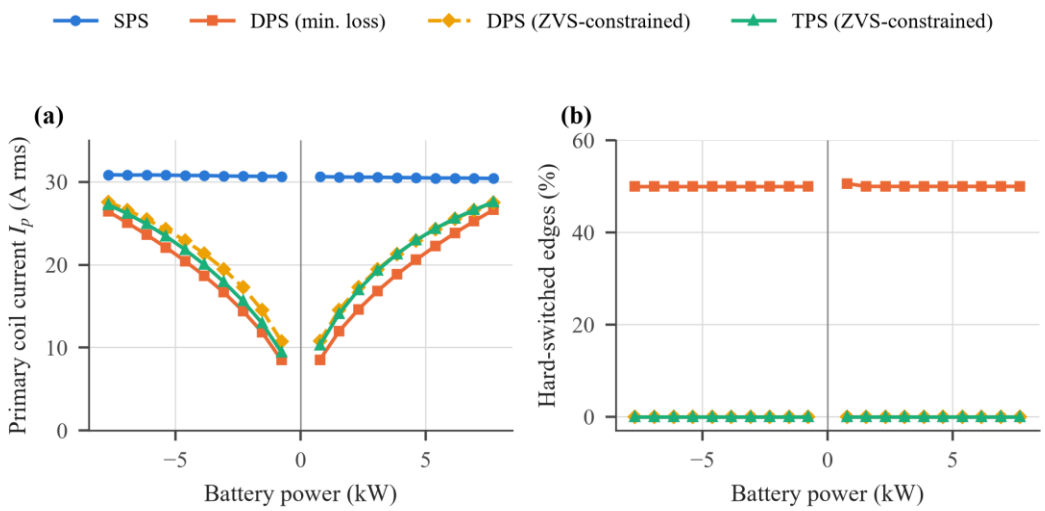


Figure 10. (a) Primary-coil RMS current and (b) fraction of hard-switched transitions versus battery power ($V_2 = 350$ V). In (b) the SPS markers coincide with the zero line of the ZVS-constrained strategies

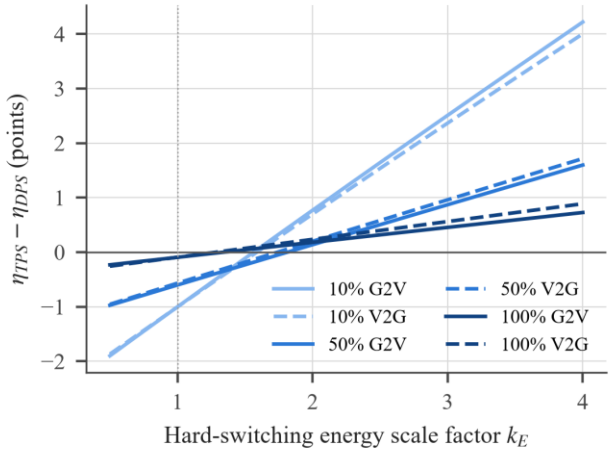


Figure 11. Efficiency advantage of TPS (ZVS-constrained) over DPS (minimum loss) as a function of the hard-switching energy scale factor k_E ($V_2 = 350$ V)

These curves assume trajectories re-optimised for the actual coupling, which requires an online estimate of k. The controller studied here does not estimate k: it uses the LUT computed for $k = 0.20$ and $V_2 = 350$ V, and the battery-power loop shifts the LUT input P_{LUT} until the battery power equals its reference. The operating points reached in this way were computed with the harmonic model from 10% to 100% load in both directions. At nominal conditions, linear interpolation between the 250-W LUT nodes changes the efficiency by less than 0.01 point and keeps the 2.0-A ZVS margin of TPS at every point. With the nominal LUT, TPS remains free of hard switching for $k = 0.175$–0.25 and for $V_2 = 300$ and 400 V, but the predicted ZVS margin falls to 0.6 A at $k = 0.25$ and to about 1.0 A at $V_2 = 300$ and 400 V, so that part of the transitions become partially soft-switched; the efficiency stays within 0.5 point of the re-optimised trajectories. At $k = 0.15$ the nominal LUT reaches only 6.7 kW in G2V, and 7.7 kW of V2G at $V_2 = 300$ V lies outside the LUT range. Full ZVS at every edge is therefore not guaranteed when the nominal LUT is used under off-nominal conditions. No hard switching occurred in any of the reported switching-level simulations, but given that the simulated edge currents are up to 1.5 A below the model prediction (Table 3), these reduced margins could lead to hard switching in hardware. A practical charger should therefore

combine power derating at low coupling with LUTs indexed by battery voltage and, if available, by an online coupling estimate.

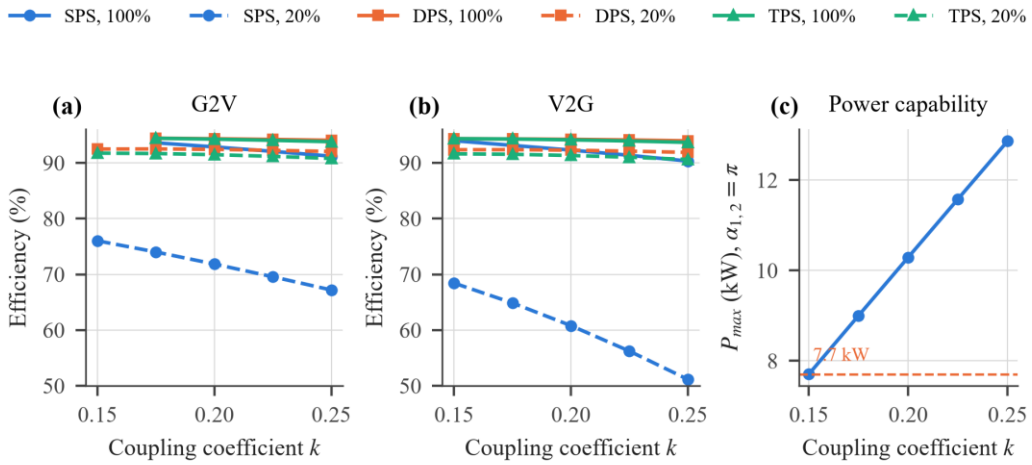


Figure 12. Effect of the coupling coefficient (misalignment) at $V_2 = 350$ V: efficiency of re-optimised trajectories at 100% and 20% of rated power in (a) G2V and (b) V2G operation; (c) maximum transferable power with $\alpha_1 = \alpha_2 = \pi$ and $\theta = 90°$

7.3. Grid-to-battery operation and power reversal

Figure 13 shows the complete grid-to-battery system with the TPS look-up table executing the dispatch profile: a ramp to 7.7 kW of charging, a reversal to 7.7 kW of V2G discharge at 0.35 s (commanded as a 5-ms ramp), a reduction to 1.54 kW of discharge at 0.65 s and a return to 1.54 kW of charging at 0.95 s. The battery power follows the reference in every interval, the DC-link voltage remains regulated at 400 V with the 100-Hz ripple predicted by (16), and θ changes sign during the reversal. The small 100-Hz modulation of the angles in Figure 13(d) is produced by the DC-link voltage feed-forward of (20), which keeps the battery-current ripple at 0.1–0.4 A peak-to-peak with TPS.

During the reversal the grid current (Figure 13(c)) shows no overcurrent, and the PLL remains synchronised. Because the DS-LCC link behaves as a current source and the battery-power controller acts directly on the modulation, the battery power settles to within 2% of the new set-point 6 ms after the start of the 15.4-kW reversal, i.e., as fast as the commanded ramp; the grid power, which depends on the DC-link controller, settles to within 5% in 22 ms, and the 10-ms average of the DC-link voltage deviates from its reference by at most 13.7 V (3.4%). These figures differ by less than 0.2 ms and 0.2 V between the three strategies, so in these simulations the choice of WPT modulation did not limit the dynamic performance of the charger. They correspond to response times far shorter than those required for primary frequency response or fast frequency reserve services, which are typically specified in seconds (Alamgir et al., 2025; Ravi & Aziz, 2022).

Table 4 compares the three strategies at system level, from the grid terminals to the battery. Following Section 6, P_{in} and P_{out} are the simulated terminal powers corrected for the post-processed switching losses, so that $\eta_{sys} = P_{out}/P_{in}$ holds for every row; the corresponding loss balance is given in Table 5. At rated power, the grid-to-battery efficiency is 90.5% with SPS in both directions, against 91.8%–92.2% with DPS and TPS. At 1.54 kW the difference is large: SPS converts only 69.8% (G2V) and 59.7% (V2G) of the energy, whereas DPS and TPS maintain 90.1%–91.3%. With SPS, for example, 2.15 kW must be drawn from the grid to deliver 1.50 kW to the battery, and in V2G only 0.94 kW of the 1.58 kW taken from the battery reaches the grid. Since aggregators frequently dispatch individual vehicles at partial power for regulation and reserve services, this difference translates directly into the energy cost of providing V2G services and into battery throughput, which affects degradation (Sagaria et al., 2025).

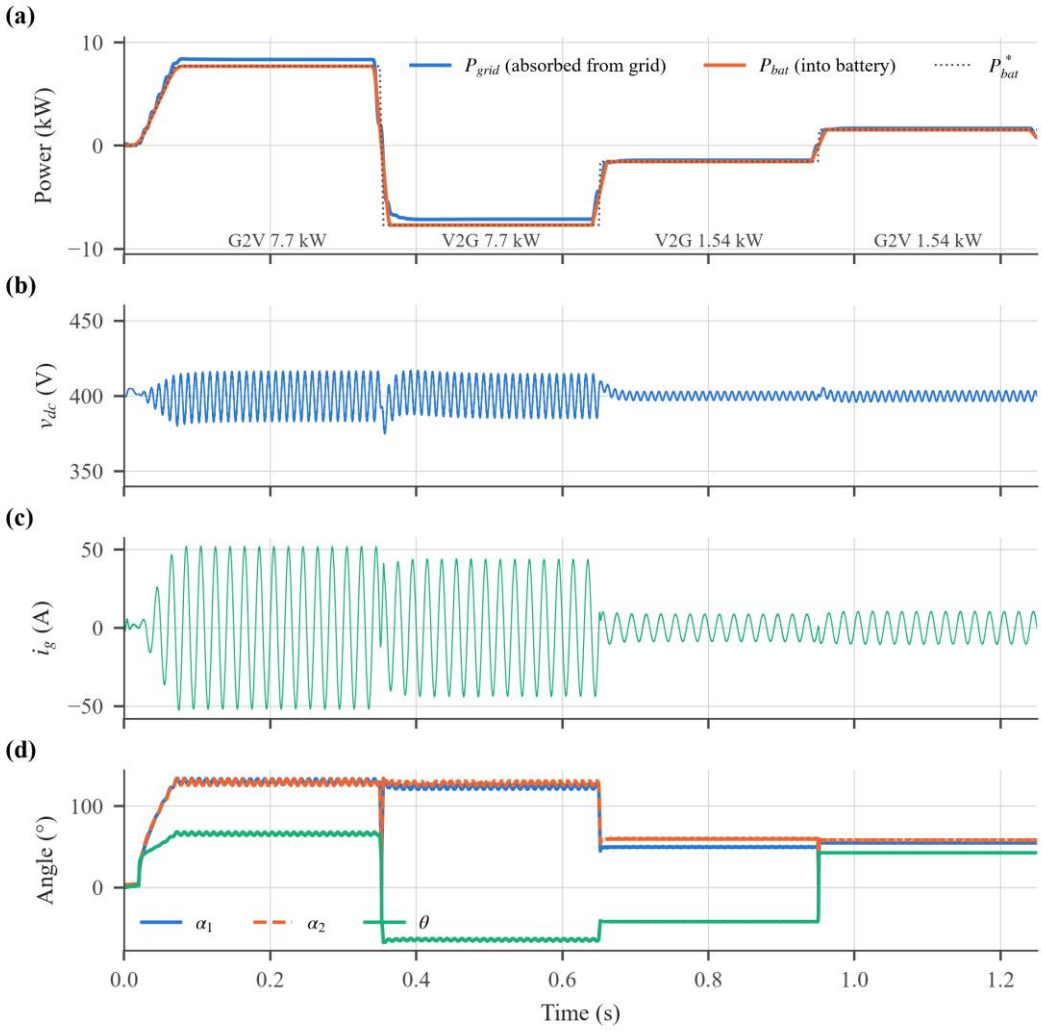


Figure 13. Full-system response to the dispatch profile with TPS modulation: (a) grid and battery power (one-cycle averages) and battery-power reference; (b) DC-link voltage; (c) grid current; (d) modulation angles

The grid-current distortion is low and nearly independent of the WPT modulation: the grid-current THD is between 0.11% and 0.51% and the TDD below 0.3% in all twelve nominal-grid operating points, the power factor is 0.999–1.000, and the residual switching-frequency current in the grid is at most 0.6 A RMS. This is a consequence of the decoupling provided by the DC link: the WPT stage draws a nearly constant DC power and affects the grid only through the small feed-forward term. The DC-link ripple scales with the apparent power as predicted by (16) (33.4–34.0 V in G2V and 30.3–30.5 V in V2G, against 33.2 V and 28.4 V calculated); the 7% excess in V2G arises because the AFE and filter losses and the reactive power of the LCL filter are not included in (16).

Loss balance. Table 5 reconciles the input and output powers of the G2V operating points component by component. The V2G points balance in the same way: at 7.7 kW the front-end loss is 116–117 W, the WPT conduction loss 430–557 W and the switching loss 36–65 W, which add up to the totals P_{loss} of Table 4. The front-end loss $P_{grid} - P_{dc,WPT}$ and the WPT conduction loss $P_{dc,WPT} - P_{bat}$ are read from the energy meters of the switching-level model, the switching losses are post-processed with (12), and their sum equals $P_{in} - P_{out}$ of Table 4. At rated power the front-end loss of 170–179 W consists of about 94 W of conduction in the AFE devices ($2R_{on}I_{Lc}^2$), 67 W in the LCL-filter inductors and 1–2.5 W in the damping resistor; at most 12 W is not allocated to a component. The WPT conduction loss is divided among the components

with the harmonic model evaluated at the logged modulation state: the coils account for 41%–45% of it, the bridge devices for 24%–25%, the compensation inductors for 17%–18% and the capacitors for 8%–10%. The model allocates all but 7–30 W (3%–7%) of the simulated WPT conduction loss. Because the two agree to within 0.4% in the stand-alone WPT simulations, this difference is attributed to the dynamic operation in the full system (the 100-Hz modulation of the operating point by the DC-link ripple feed-forward and the 20-kHz update of the modulation angles), which the steady-state model does not represent. With SPS, the WPT conduction loss of 552–563 W is almost independent of the power and is about 5% higher than the fundamental-frequency estimate of 529 W from (7), which neglects the higher-order current harmonics.

Table 4. Grid-to-battery performance of the three modulation strategies (full switching-level simulation, nominal grid). P_{in}: power drawn from the grid (G2V) or the battery (V2G); P_{out}: power delivered to the battery (G2V) or the grid (V2G); both include the post-processed switching losses (Section 6); $P_{loss} = P_{in} - P_{out}$ and $\eta_{sys} = P_{out}/P_{in}$ hold for the displayed values; THD_I and TDD up to the 50th harmonic, TDD referred to $I_L = 33.5$ A; ΔV_{dc}: peak-to-peak DC-link ripple

Strategy	Operating point	P_{in} (W)	P_{out} (W)	P_{loss} (W)	η_{sys} (%)	THD_I (%)	TDD (%)	PF	ΔV_{dc} (V)
SPS	G2V 7.7 kW	8474.9	7668.1	806.8	90.5	0.25	0.27	1.000	34.0
	V2G 7.7 kW	7730.3	6992.1	738.2	90.5	0.27	0.25	1.000	30.3
	V2G 1.54 kW	1577.0	940.7	636.3	59.7	0.51	0.07	0.999	4.9
	G2V 1.54 kW	2144.5	1496.5	648.0	69.8	0.49	0.14	1.000	9.4
DPS	G2V 7.7 kW	8355.6	7679.0	676.6	91.9	0.21	0.23	1.000	33.4
	V2G 7.7 kW	7723.1	7119.8	603.3	92.2	0.11	0.10	1.000	30.5
	V2G 1.54 kW	1560.1	1422.9	137.2	91.2	0.30	0.06	1.000	6.1
	G2V 1.54 kW	1668.8	1523.5	145.3	91.3	0.17	0.04	1.000	7.0
TPS	G2V 7.7 kW	8374.7	7689.7	685.0	91.8	0.12	0.14	1.000	33.5
	V2G 7.7 kW	7711.7	7102.3	609.4	92.1	0.12	0.11	1.000	30.4
	V2G 1.54 kW	1548.0	1395.4	152.6	90.1	0.22	0.04	1.000	6.0
	G2V 1.54 kW	1695.0	1529.5	165.5	90.2	0.28	0.06	1.000	7.1

Table 5. Loss balance of the G2V operating points (W, full switching-level simulation, nominal grid). Front end: $P_{grid} - P_{dc,WPT}$; WPT: $P_{dc,WPT} - P_{bat}$ (both simulated); devices, L_f, coils and capacitors: allocation of the WPT conduction loss by the harmonic model; dyn.: simulated minus allocated; Sw.: post-processed switching losses of the AFE and of bridges B1 and B2; total $= P_{in} - P_{out}$ of Table 4

Strategy	P_{bat} (kW)	Front end	WPT	Devices	L_f	Coils	Caps	Dyn.	Sw. AFE	Sw. B1	Sw. B2	Total
SPS	7.7	179	563	141	101	250	51	20	13	27	25	807
	1.54	22	552	140	100	249	44	18	4	36	34	648
DPS	7.7	170	451	107	76	192	46	30	13	22	21	677
	1.54	9	95	23	17	39	9	7	3	19	19	145
TPS	7.7	171	477	114	81	205	46	30	13	13	12	685
	1.54	10	132	33	23	56	11	9	3	11	10	166

7.4. Four-quadrant active- and reactive-power capability

Figure 14 and Table 6 show the operation of the charger in all four quadrants of the P–Q plane, with a battery power of ± 5 kW and reactive-power commands of ± 4 kvar. The reactive power at the PCC tracks its reference to within 0.3% in every quadrant, and the transitions between quadrants are completed within one to two fundamental cycles; the brief spikes in the reactive-power trace at the active-power reversals are artefacts of the quarter-cycle-delay estimator used for plotting, not of the converter. All operating points lie well inside the 9.2-kVA capability circle of the AFE, and the grid-current THD remains between 0.12% and 0.18%.

Table 6. Steady-state four-quadrant operating points (TPS; $P_{grid} > 0$ absorbed, $Q_{grid} > 0$ injected)

Point	Mode	P_{grid} (kW)	Q_{grid} (kvar)	PF	THD_I (%)	ΔV_{dc} (V)	I_g (A)
A	G2V, unity PF	+5.42	−0.01	1.000	0.18	22.0	23.7
B	G2V + Q injection	+5.46	+3.99	0.807	0.15	27.8	29.5
C	V2G + Q injection	−4.59	+4.01	0.753	0.14	26.2	26.3
D	V2G + Q absorption	−4.58	−3.99	0.754	0.12	24.4	26.3
E	G2V + Q absorption	+5.46	−4.01	0.807	0.14	27.0	29.7

Two observations are important for the grid-service value of the charger. First, reactive power is produced entirely by the AFE and the DC-link capacitor: the battery power remains at 5.00 kW in every quadrant, so voltage-support services can be offered without cycling the battery and therefore without additional battery degradation. The cost is a small increase of the grid-side conduction losses, which reduces the grid-to-battery efficiency from 91.6% at unity power factor to 90.8%–91.0% at a power factor of 0.75–0.81. Second, the DC-link ripple increases with the apparent power, from 22.0 V at 5.4 kVA to 24.4–27.8 V at 6.1–6.8 kVA, in agreement with (16) (21.6 V and 24.2–27.0 V calculated); the DC-link capacitor must therefore be sized for the apparent-power rating of the grid-support functions, not only for the active-power rating of the charger, as also noted by Kisacikoglu et al. (2013).

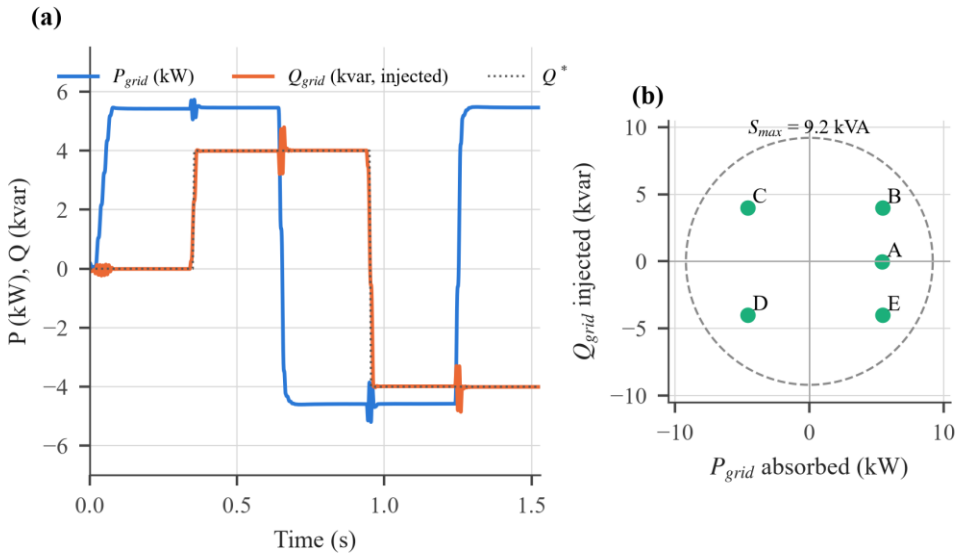


Figure 14. Four-quadrant operation (TPS, $P_{bat} = \pm 5$ kW, $Q^* = \pm 4$ kvar): (a) active and reactive power at the PCC; (b) steady-state operating points A–E in the P–Q plane with the AFE capability limit

7.5. Frequency support

Figure 15 shows the response of the charger, scheduled to charge at 3.85 kW, to an under-frequency event (50 Hz to 49.0 Hz at 0.30 s) followed by an over-frequency event (to 50.5 Hz at 0.70 s), with the frequency-watt function (25) enabled. According to (25), the 49.0-Hz event should change the battery power by $-(1.0 - 0.036)/(0.03 \times 50) \times 7.7$ kW $= -4.95$ kW, i.e., from 3.85 kW of charging to 1.10 kW of V2G discharge, and the 50.5-Hz event should raise the charging power to 6.23 kW. The simulated steady-state battery powers are -1.097 kW and $+6.232$ kW, within 3 W of these values, so the charger automatically stops charging and starts exporting power during the under-frequency event without any external command. The new power level is reached within 39–40 ms (5% band), a time dominated by the PLL and the 10-Hz frequency filter, which is well within the sub-second response times required for fast frequency services.

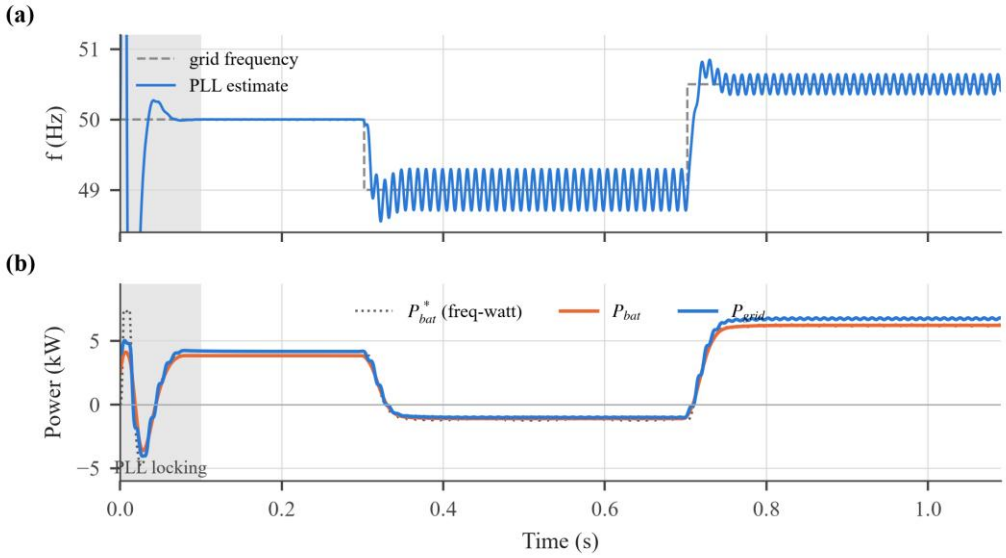


Figure 15. Frequency-watt response (TPS, scheduled charging 3.85 kW, droop 3%): (a) grid frequency and PLL estimate; (b) battery-power reference, battery power and grid power. The shaded interval is the PLL locking period at start-up

Two practical issues are also revealed by this test. First, because the SOGI of (21) is tuned to 50 Hz, off-nominal frequencies leave a 100-Hz oscillation on the frequency estimate (0.59 Hz peak-to-peak at 49.0 Hz, mean correct to within 3 mHz), which becomes a 150–320-W ripple on the battery-power reference; a frequency-adaptive SOGI with a frequency-locked loop (Golestan et al., 2017) would remove it. Second, before the PLL has locked at start-up the frequency-watt function produced a spurious power transient, so the grid-support functions should be interlocked with a PLL lock detector.

7.6. Weak-feeder operation and volt-var support

Voltage support matters most at the end of long, weak low-voltage feeders, where the active power of a 7.7-kW charger is enough to move the voltage by several percent. This case was studied with a Thevenin grid impedance of $R_{grid} = 0.4\ \Omega$ and $L_{grid} = 1.2$ mH ($X_{grid} = 0.377\ \Omega$, $X/R = 0.94$, short-circuit ratio 12.5 with respect to 7.7 kVA), with the charger first charging and then discharging at 7.7 kW.

Influence of the grid-voltage feed-forward. With the default controller, which feeds forward the anti-aliased measured PCC voltage, the charger did not reach a normal operating point on this feeder. As shown in Figure 16, a sustained oscillation at about 1.85 kHz appeared on the PCC voltage and on the grid current, the modulation index was saturated during 18% of the samples and the DC-link voltage could not be held at its reference (333 V instead of 400 V in G2V). In G2V the grid-current THD was 17.5%–19.7% and the voltage THD 45%–50%, with and without the volt-var function. The small-signal analysis of Section 5 predicts a stable current loop for this grid inductance, so this is a large-signal phenomenon: the energisation of the weak feeder excites the filter resonance, the raw feed-forward copies the high-frequency PCC voltage into the converter voltage reference and drives the modulator into saturation, and the current controller, having lost authority, sustains a limit cycle. With the SOGI fundamental v_α as feed-forward, operation is normal from start-up (grid-current THD 0.20%, peak modulation index 0.75, no saturation), and all weak-feeder results below use it. Because the raw feed-forward is advantageous on stiff grids, where it rejects the grid-voltage harmonics (Section 7.7), a practical controller should select the feed-forward according to the grid strength or use a band-limited version of it.

Feeder voltage. With V_p the PCC voltage phasor taken as the reference, P the active power absorbed by the charger and Q the reactive power injected into the grid, the feeder imposes

$$\underline{V_s} = V_p + \frac{R_{grid}P - X_{grid}Q}{V_p} + \mathrm{j}\,\frac{X_{grid}P + R_{grid}Q}{V_p}, \qquad \frac{\partial V_p}{\partial Q} \approx \frac{X_{grid}}{V_p}, \qquad \frac{\partial V_p}{\partial P} \approx -\frac{R_{grid}}{V_p}, \tag{29}$$

with $|\underline{V_s}| = 230$ V. Solving (29) for V_p with the simulated P and Q reproduces the simulated PCC voltages to within 0.01 V (Table 7). Without volt-var, charging at 7.7 kW lowers the PCC voltage to 0.930 p.u., and V2G export raises it to 1.050 p.u.

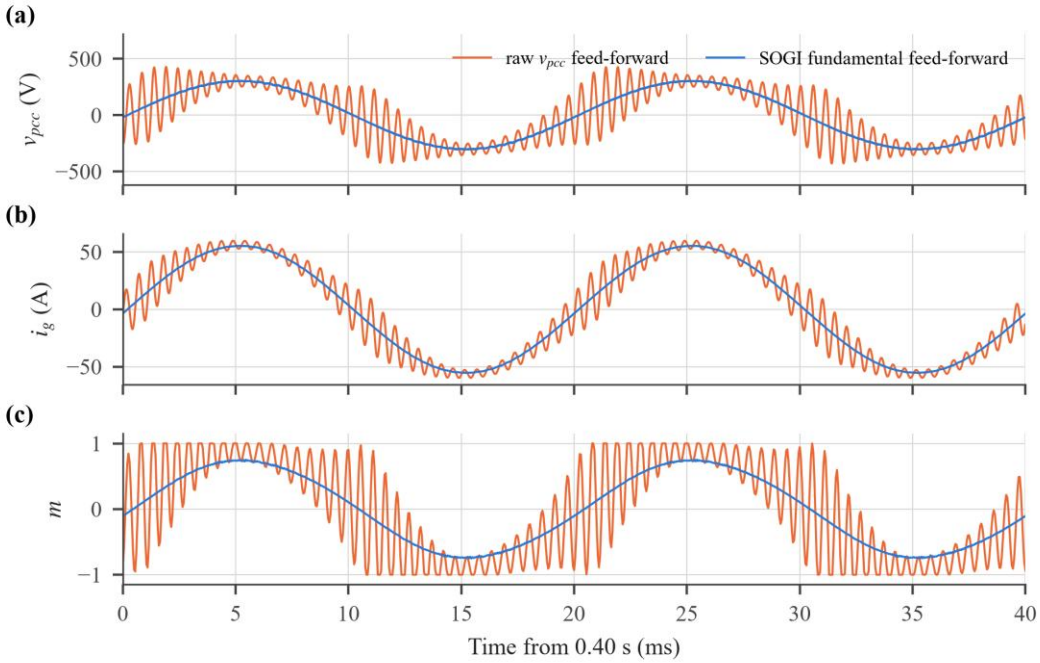


Figure 16. Weak feeder ($R_{grid} = 0.4\ \Omega$, $L_{grid} = 1.2$ mH), G2V at 7.7 kW: (a) PCC voltage, (b) grid current and (c) AFE modulation index with the raw PCC-voltage feed-forward (saturated limit cycle) and with the SOGI fundamental as feed-forward

Table 7. Weak-feeder operation at ± 7.7 kW with and without volt-var (VV) (TPS, SOGI feed-forward). V_{pcc} (sim.): simulated; V_{pcc} (29): calculated from the simulated P_{grid} and Q_{grid}; $P_{grid} > 0$ absorbed, $Q_{grid} > 0$ injected

Mode	VV	V_{pcc} sim. (p.u.)	V_{pcc} (29) (p.u.)	P_{grid} (kW)	Q_{grid} (kvar)	P_{bat} (kW)	I_g (A)	PF	THD_I (%)	η_{sys} (%)
G2V	off	0.930	0.930	+8.37	−0.02	+7.70	39.2	1.000	0.20	91.6
V2G	off	1.050	1.050	−7.13	+0.02	−7.70	29.5	1.000	0.18	92.2
G2V	on	0.945	0.945	+8.31	+1.90	+7.64	39.2	0.975	0.22	91.5
V2G	on	1.041	1.041	−7.13	−1.26	−7.70	30.2	0.985	0.16	92.1

Volt-var response. Figure 17 and Table 7 show the effect of the IEEE Std 1547-2018 Category B volt-var characteristic. During charging, the charger injects 1.90 kvar and raises the PCC voltage from 0.930 to 0.945 p.u. During V2G export, it absorbs 1.26 kvar and lowers the voltage from 1.050 to 1.041 p.u. These equilibria agree with the intersection of the volt-var characteristic with (29), which gives 0.945 p.u. with 1.96 kvar and 1.042 p.u. with -1.22 kvar. The 3.5% difference in reactive power comes from a 0.15% error of the filtered PLL voltage estimate, amplified by the steep slope of the characteristic. After the power reversal, the reactive power settles to within 5% of its final value in 104 ms, which is dominated by the 5-Hz voltage filter and is well within the default 5-s open-loop response time of IEEE Std 1547-2018. In G2V the current limit (26) is active: to give priority to the reactive power, the supervisor reduces the battery power from 7.70 to 7.64

kW, which is exactly the value $0.9\sqrt{(I_{max}V_{pcc,rms})^2 - Q^{*2}} = 7.64$ kW. The volt-var function costs almost nothing in efficiency (0.03–0.08 points) and causes no battery cycling.

The magnitude of this support is limited by the feeder rather than by the controller: by (29), cancelling the voltage change of an active power P would require $Q \approx (R_{grid}/X_{grid})P \approx 1.06P$, more than 8 kvar at rated power, which exceeds both the 0.44-p.u. limit of the characteristic and the current rating. A single charger can therefore only mitigate the voltage change caused by its own active power; here the V2G voltage returns inside the $\pm 5\%$ band and the G2V shortfall falls from 2.0 to 0.5 points. Larger corrections require volt-watt curtailment or the aggregated reactive power of many chargers.

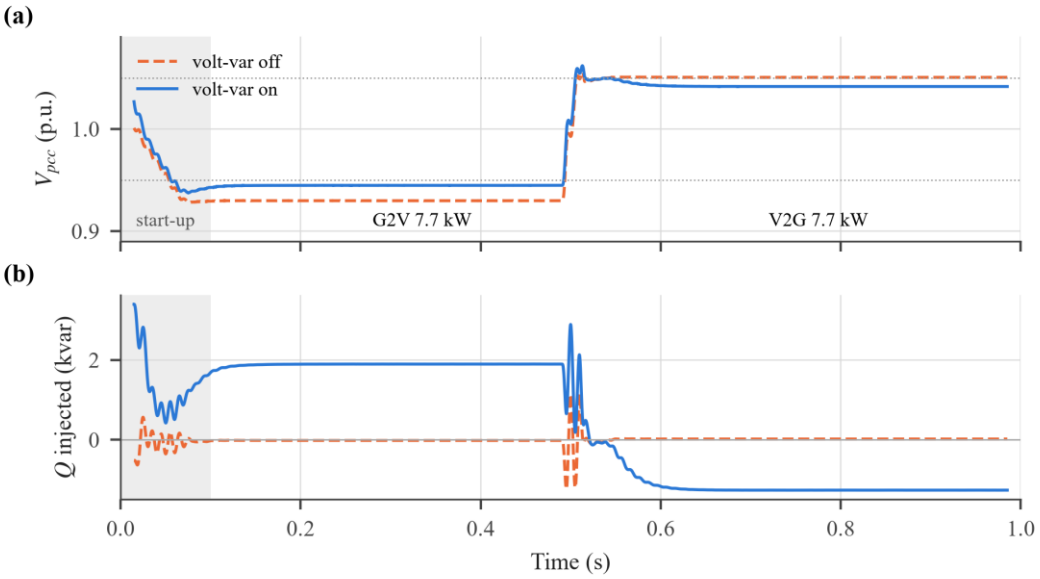


Figure 17. Weak feeder, G2V 7.7 kW followed by V2G 7.7 kW (TPS, SOGI feed-forward), with and without volt-var: (a) RMS PCC voltage (one-cycle values); (b) reactive power injected into the grid. The dotted lines mark $\pm 5\%$; the shaded interval is the start-up

7.7. Power quality with a distorted grid voltage

Distribution grids are rarely sinusoidal, so the charger was also tested at rated power in both directions with a background voltage distortion of 3% 3rd, 4% 5th and 2.5% 7th harmonic (THD_v = 5.6%), with the harmonic compensators (HC) of (24) disabled and enabled. The results are compared with the ideal-grid case in Table 8 and Figure 18, against the current-distortion limits of IEEE Std 519-2022 and IEEE Std 1547-2018 (IEEE, 2018, 2022). These limits depend on the ratio I_{sc}/I_L at the PCC; the most stringent category, $I_{sc}/I_L < 20$ (4.0% for each odd harmonic below the 11th and a TDD of 5.0%), is used throughout, which is conservative for the nominal grid ($I_{sc}/I_L \approx 116$) and applies directly to the weak feeder of Section 7.6 ($I_{sc}/I_L = 12.5$). The TDD is referred to $I_L = 33.5$ A, the rated current of the charger, taken as its maximum demand current. Harmonics up to the 50th are evaluated over ten-cycle windows; the 3-s and 10-min aggregation and percentile assessment of IEEE Std 519-2022, the type-test procedures that accompany IEEE Std 1547-2018 and the R_{sce}-dependent limits of IEC 61000-3-12 (International Electrotechnical Commission, 2021) were not applied. The results below therefore show whether the simulated distortion lies within the IEEE limits; they are not a compliance assessment.

On the ideal grid, the grid-current THD is 0.12% and the TDD at most 0.14%, with every harmonic below 0.07% of I_L. The distorted grid voltage increases the current distortion, but much less than might be expected: even without harmonic compensation, the TDD is only 0.76% in G2V and 0.32% in V2G, and

the largest individual harmonic, the 5th, is 0.57% of I_L, i.e., seven times below its limit. The reason is the feed-forward of the measured PCC voltage in the converter voltage reference, which reproduces the grid-voltage harmonics at the converter terminals and therefore prevents them from driving harmonic currents through the filter. The power factor of 0.998 in the distorted cases is not caused by the charger: it equals $1/\sqrt{1+\mathrm{THD}_v^2}$ for a sinusoidal current in phase with the fundamental of a voltage with 5.6% THD.

Table 8. Grid-current distortion at rated power (± 7.7 kW, TPS). Harmonic currents I_h and TDD in % of $I_L = 33.5$ A; HC: harmonic compensators of (24)

Grid voltage	Mode	THD_v (%)	THD_I (%)	TDD (%)	I_3	I_5	I_7	PF
ideal grid	G2V	0.02	0.12	0.14	0.04	0.07	0.01	1.000
ideal grid	V2G	0.01	0.12	0.11	0.05	0.04	0.01	1.000
distorted, HC off	G2V	5.65	0.69	0.76	0.33	0.57	0.35	0.998
distorted, HC off	V2G	5.55	0.35	0.32	0.21	0.19	0.08	0.998
distorted, HC on	G2V	5.65	0.53	0.58	0.28	0.43	0.24	0.998
distorted, HC on	V2G	5.54	0.45	0.41	0.22	0.29	0.15	0.998
Limit		–	–	5.0	4.0	4.0	4.0	–

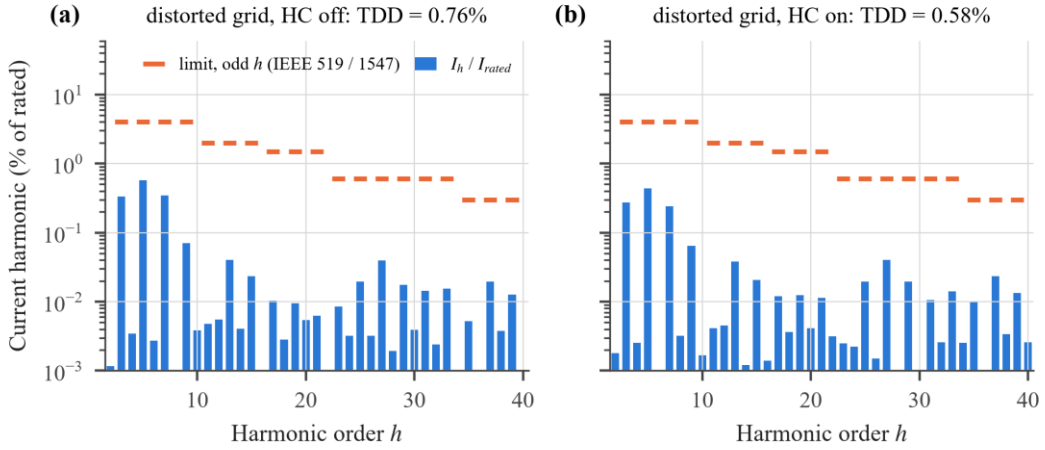


Figure 18. Harmonic spectrum of the grid current in G2V operation at 7.7 kW with a distorted grid voltage (THD_v = 5.6%): (a) harmonic compensators disabled; (b) enabled. The dashes mark the IEEE Std 519-2022 / IEEE Std 1547-2018 limits for the odd harmonics

Enabling the harmonic compensators reduces the G2V distortion further (TDD from 0.76% to 0.58%, I_5 from 0.57% to 0.43%), but slightly increases it in V2G (TDD from 0.32% to 0.41%). With the compensators enabled, the 3rd, 5th and 7th harmonics of the grid current (0.28%, 0.43% and 0.24% of I_L in G2V) coincide with those of the reference i_g^* (0.28%, 0.41% and 0.22%): the compensators eliminate the tracking error, as designed, and the residual distortion originates in the reference itself, because the distorted PCC voltage leaves small harmonic ripples on the PLL estimates that (23) converts into current harmonics. A multiple-SOGI or harmonic-decoupled synchronisation stage would remove them; with the present controller, the simulated distortion is below every assessed limit by a factor of more than six, so the harmonic compensators were not needed to meet these limits under the simulated conditions.

7.8. Role of the DC-link power feed-forward

The last scenario repeats the full G2V-to-V2G reversal of Section 7.3 without the power feed-forward term P_{ff} of (22). For a fair comparison, the integrator range of the DC-link controller was extended in this case from ± 3 kW, which is sufficient when P_{ff} carries the power, to $\pm 1.2 S_r$, so that the PI controller alone can carry the full power. As Figure 19 shows, the battery power is unaffected, because it is set by the WPT controller, but the DC-link voltage must now absorb the 15.4-kW power step until the PI controller has

reversed the grid power. The 10-ms average DC-link voltage deviates by 155 V (39%) from its reference, against 13.7 V with feed-forward. The instantaneous voltage reaches 565 V, and the voltage takes 295 ms instead of 6.7 ms to return within $\pm 2\%$ of 400 V. The deviation is consistent with the bound $\Delta P/K_{pv} = 15.4\ \text{kW}/75.4\ \text{W/V} = 204$ V of a purely proportional loop. Such an overvoltage would exceed the rating of typical 450-V DC-link capacitors, so without power feed-forward the reversal would have to be slowed to a few hundred milliseconds or the DC-link capacitance increased several times; the feed-forward of the measured WPT power is what allows the charger to exploit the fast reversal of the DS-LCC link for grid services.

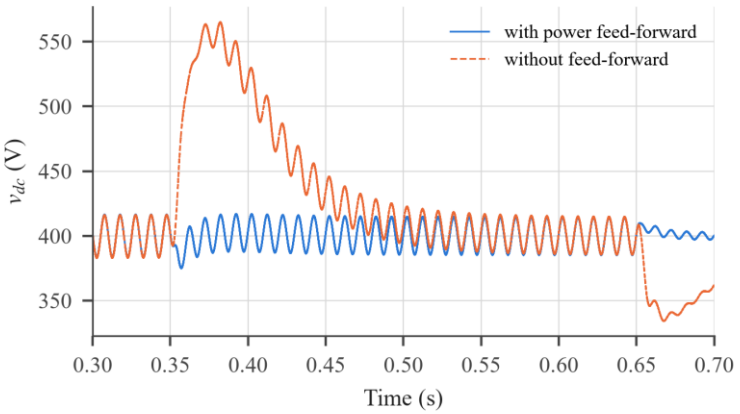


Figure 19. DC-link voltage during the G2V-to-V2G reversal (7.7 kW to -7.7 kW at 0.355 s) and the step to -1.54 kW at 0.652 s, with and without the WPT power feed-forward (TPS)

8. Discussion, Limitations and Practical Implications

8.1. Can a bidirectional wireless charger provide useful grid support?

The results allow the V2G services listed in the literature (Alamgir et al., 2025; Kempton & Tomić, 2005; Ravi & Aziz, 2022; Yilmaz & Krein, 2013) to be assessed one by one for the charger studied here. Efficiency at partial power, however, is critical: with SPS, providing 1.54 kW of V2G costs 40% of the energy taken from the battery, so the modulation strategy is a prerequisite for economically useful V2G operation. Reactive power is supplied by the grid-side converter without battery energy, so the modest volt-var support of a single charger can be offered continuously by any vehicle parked over a pad. Under the simulated conditions the charger caused very little harmonic distortion; active harmonic filtering by the AFE (Yilmaz & Krein, 2013) was not evaluated.

8.2. Choice of modulation strategy

SPS is unsuitable for partial-power V2G operation. Between DPS and TPS the efficiency differences are small (below about 1 point), whereas minimum-loss DPS hard-switches half of the transitions and ZVS-constrained TPS avoided hard switching at every simulated operating point, with partial ZVS at part of the edges (Table 3). TPS is therefore preferred for the charger studied; its look-up tables add no real-time complexity and can be recomputed for other devices or coils with the procedure of Figure 4.

8.3. Limitations and future work

The findings are based on switching-level simulations and an analytical model cross-validated against them; no hardware experiment was performed, so the reported efficiencies, ZVS margins and response times have not been verified experimentally. The device switching energies are representative rather than device-specific (Section 7.2), and the simulated ZVS margins are smaller than the model predicts (Table 3). Pad core and shielding losses, frequency-dependent winding resistances, gate-drive, auxiliary and interconnection losses

were not modelled, so the efficiencies are upper bounds. Thermal constraints were not considered: the on-state resistance of SiC MOSFETs rises with junction temperature, which would increase the device conduction losses (about 25% of the WPT conduction loss and 55% of the front-end loss at rated power, Table 5), and component temperatures may require derating at high ambient temperature. Component tolerances, detuning and time-varying coupling were not studied, and the battery was a constant EMF behind a resistance. The communication delay between the ground and vehicle controllers was not included; if the battery-power loop is closed over the wireless link, delays of several milliseconds would require a lower loop bandwidth and lengthen the 6-ms battery-side reversal (Bertoluzzo et al., 2023). Finally, a single charger on a single-phase supply was studied, and bidirectional wireless charging is not yet standardised (SAE International, 2024). Future work will address hardware validation, controller-in-the-loop tests with communication delays, thermal and tolerance analysis and online coupling estimation.

9. Conclusions

This paper has presented a simulation study of a 7.7-kW, 85-kHz bidirectional DS-LCC wireless charger connected to a 230-V, 50-Hz single-phase grid. The main conclusions are:

1) With SPS control, the coil and bridge currents are fixed by the bridge voltages, so the WPT conduction loss is 530–560 W at any power level and the light-load efficiency collapses (56.9% in G2V and 20.9% in V2G at 10% load).
2) The multi-harmonic model agrees with 240 switching-level operating points to within 0.26% in power on average (maximum 3.5%, or 1.6% above 1.5 kW).
3) DPS and TPS reduce the light-load losses by a factor of seven to nine and keep the DC-DC efficiency between about 89% and 94.4% from 10% to 100% load; ZVS-constrained TPS avoided hard switching at all simulated points, although part of the edges switched with partial ZVS, and becomes the more efficient option when the hard-switching energy exceeds 1.3–1.8 times the nominal value.
4) With losses reconciled from grid to battery, the charger reaches 91.8%–92.2% efficiency at rated power with DPS or TPS, reverses the 15.4-kW range within 22 ms at the grid, and keeps the simulated grid-current TDD below 0.3% in the nominal-grid dispatch scenarios and at or below 0.76% under the tested distorted-grid conditions, within the assessed IEEE current-distortion limits (not a formal compliance assessment).
5) In simulation, the charger provided frequency-watt response within 40 ms, four-quadrant reactive power without battery cycling and volt-var support on a weak feeder, enabled by DC-link power feed-forward and, on weak feeders, a fundamental-only grid-voltage feed-forward.

These results indicate that bidirectional DS-LCC wireless chargers can act as efficient and grid-friendly V2G resources; hardware validation is needed to confirm them.

Declaration of Ethical Standards

As the authors of this study, we declare that we comply with all ethical standards.

Credit Authorship Contribution Statement

V. Ogunyemi: Conceptualization, Methodology, Software, Validation, Formal analysis, Investigation, Writing – Original Draft, Visualization.

T. Lawal: Writing – Review & Editing, Supervision.

Declaration of Competing Interest

The authors declared that they have no conflict of interest.

Acknowledgements

Not applicable.

Funding

This research did not receive any specific grant from funding agencies in the public, commercial, or not-for-

profit sectors.

Data Availability

The MATLAB/Simulink model-generation scripts, the Python analysis scripts, the processed simulation data that support the findings and the raw simulation records are available from the corresponding author on reasonable request.

References

Alamgir, S., Hassan, S. J. U., Mehdi, A., Abdelmaksoud, A., Haider, Z., Shin, G., & Kim, C. (2025). A comprehensive review of vehicle-to-grid (V2G) technology as an ancillary services provider. *Results in Engineering, 27*, Article 106813. https://doi.org/10.1016/j.rineng.2025.106813

Amjad, M., Farooq-i-Azam, M., Ni, Q., Dong, M., & Ansari, E. A. (2022). Wireless charging systems for electric vehicles. *Renewable and Sustainable Energy Reviews, 167*, Article 112730. https://doi.org/10.1016/j.rser.2022.112730

Bamigbade, A., Umesh, B. S., Khadkikar, V., El Moursi, M. S., Zeineldin, H. H., & Al Hosani, M. (2022). Reduced-order generalized integrator-based phase-locked loop: Performance improvement for grid synchronization of single-phase inverters. *IEEE Transactions on Power Delivery, 37*(5), 4382–4393. https://doi.org/10.1109/TPWRD.2022.3169470

Bertoluzzo, M., Kumar, A., & Sagar, A. (2023). Control strategy for a bidirectional wireless power transfer system with vehicle to home functionality. *IEEE Access, 11*, 60421–60448. https://doi.org/10.1109/ACCESS.2023.3286302

Bhattacharjee, A. K., & Batarseh, I. (2020). Optimum hybrid modulation for improvement of efficiency over wide operating range for triple-phase-shift dual-active-bridge converter. *IEEE Transactions on Power Electronics, 35*(5), 4804–4818. https://doi.org/10.1109/TPEL.2019.2943392

Ciobotaru, M., Teodorescu, R., & Blaabjerg, F. (2006). A new single-phase PLL structure based on second order generalized integrator. In *2006 37th IEEE Power Electronics Specialists Conference* (pp. 1–6). IEEE. https://doi.org/10.1109/PESC.2006.1711988

ElGhanam, E., Hassan, M., & Osman, A. (2021). Design of a high power, LCC-compensated, dynamic, wireless electric vehicle charging system with improved misalignment tolerance. *Energies, 14*(4), Article 885. https://doi.org/10.3390/en14040885

Fu, N., Deng, J., Wang, Z., & Chen, D. (2023). Dual-phase-shift control strategy with switch-controlled capacitor for overall efficiency optimization in wireless power transfer system. *IEEE Transactions on Vehicular Technology, 72*(6), 7304–7317. https://doi.org/10.1109/TVT.2023.3241695

Golestan, S., Guerrero, J. M., & Vasquez, J. C. (2017). Single-phase PLLs: A review of recent advances. *IEEE Transactions on Power Electronics, 32*(12), 9013–9030. https://doi.org/10.1109/TPEL.2017.2653861

Huang, J., He, X., Huo, P., & Xu, R. (2024). A hybrid modulation strategy for LCC–LCC compensated bidirectional wireless power transfer system to achieve high efficiency in the whole operating range. *IEEE Transactions on Industrial Electronics, 71*(1), 327–337. https://doi.org/10.1109/TIE.2023.3247774

IEEE. (2018). *IEEE standard for interconnection and interoperability of distributed energy resources with associated electric power systems interfaces* (IEEE Std 1547-2018). https://doi.org/10.1109/IEEESTD.2018.8332112

IEEE. (2022). *IEEE standard for harmonic control in electric power systems* (IEEE Std 519-2022). https://doi.org/10.1109/IEEESTD.2022.9848440

International Electrotechnical Commission. (2021). *Electromagnetic compatibility (EMC) — Part 3-12: Limits — Limits for harmonic currents produced by equipment connected to public low-voltage systems with input current >16 A and ≤75 A per phase* (IEC Standard No. 61000-3-12:2011+AMD1:2021 CSV). https://webstore.iec.ch/en/publication/69084

International Electrotechnical Commission. (2024). *Electromagnetic compatibility (EMC) — Part 3-2: Limits — Limits for harmonic current emissions (equipment input current ≤16 A per phase)* (IEC Standard No. 61000-3-2:2018+AMD1:2020+AMD2:2024 CSV). https://webstore.iec.ch/en/publication/92799

International Energy Agency. (2025). *Global EV outlook 2025*. https://www.iea.org/reports/global-ev-outlook-2025

International Organization for Standardization. (2022). *Road vehicles — Vehicle to grid communication interface — Part 20: 2nd generation network layer and application layer requirements* (ISO Standard No. 15118-20:2022). https://www.iso.org/standard/77845.html

Jiang, Y., Wang, L., Fang, J., Li, R., Han, R., & Wang, Y. (2021). A high-efficiency ZVS wireless power transfer system for electric vehicle charging with variable angle phase shift control. *IEEE Journal of Emerging and Selected Topics in Power Electronics, 9*(2), 2356–2372. https://doi.org/10.1109/JESTPE.2020.2984575

Kempton, W., & Tomić, J. (2005). Vehicle-to-grid power implementation: From stabilizing the grid to supporting large-scale renewable energy. *Journal of Power Sources, 144*(1), 280–294. https://doi.org/10.1016/j.jpowsour.2004.12.022

Kisacikoglu, M. C., Ozpineci, B., & Tolbert, L. M. (2013). EV/PHEV bidirectional charger assessment for V2G reactive power operation. *IEEE Transactions on Power Electronics, 28*(12), 5717–5727. https://doi.org/10.1109/TPEL.2013.2251007

Krismer, F., & Kolar, J. W. (2012). Closed form solution for minimum conduction loss modulation of DAB converters. *IEEE Transactions on Power Electronics, 27*(1), 174–188. https://doi.org/10.1109/TPEL.2011.2157976

Li, S., Li, W., Deng, J., Nguyen, T. D., & Mi, C. C. (2015). A double-sided LCC compensation network and its tuning method for wireless power transfer. *IEEE Transactions on Vehicular Technology, 64*(6), 2261–2273. https://doi.org/10.1109/TVT.2014.2347006

Li, S., & Lin, H. (2022). A capacitor-current-feedback positive active damping control strategy for LCL-type grid-connected inverter to achieve high robustness. *IEEE Transactions on Power Electronics, 37*(6), 6462–6474. https://doi.org/10.1109/TPEL.2021.3137845

Li, S., Lu, S., & Mi, C. C. (2021). Revolution of electric vehicle charging technologies accelerated by wide bandgap devices. *Proceedings of the IEEE, 109*(6), 985–1003. https://doi.org/10.1109/JPROC.2021.3071977

Li, S., & Mi, C. C. (2015). Wireless power transfer for electric vehicle applications. *IEEE Journal of Emerging and Selected Topics in Power Electronics, 3*(1), 4–17. https://doi.org/10.1109/JESTPE.2014.2319453

Liserre, M., Blaabjerg, F., & Hansen, S. (2005). Design and control of an LCL-filter-based three-phase active rectifier. *IEEE Transactions on Industry Applications, 41*(5), 1281–1291. https://doi.org/10.1109/TIA.2005.853373

Liu, Y., Madawala, U. K., Mai, R., & He, Z. (2020). An optimal multivariable control strategy for inductive power transfer systems to improve efficiency. *IEEE Transactions on Power Electronics, 35*(9), 8998–9010. https://doi.org/10.1109/TPEL.2020.2970780

Lu, J., Sun, S., Ke, H., & Zhu, G. (2024). Triple phase shift modulation scheme for bidirectional wireless power transfer systems with efficiency maximization. *IEEE Transactions on Circuits and Systems II: Express Briefs, 71*(12), 5029–5033. https://doi.org/10.1109/TCSII.2024.3420095

Madawala, U. K., & Thrimawithana, D. J. (2011). A bidirectional inductive power interface for electric vehicles in V2G systems. *IEEE Transactions on Industrial Electronics, 58*(10), 4789–4796. https://doi.org/10.1109/TIE.2011.2114312

Mahesh, A., Chokkalingam, B., & Mihet-Popa, L. (2021). Inductive wireless power transfer charging for electric vehicles—A review. *IEEE Access, 9*, 137667–137713. https://doi.org/10.1109/ACCESS.2021.3116678

Mohammad, M., Onar, O. C., Su, G.-J., Pries, J., Galigekere, V. P., Anwar, S., Asa, E., Wilkins, J., Wiles, R., White, C. P., & Seiber, L. E. (2021). Bidirectional LCC–LCC-compensated 20-kW wireless power transfer system for medium-duty vehicle charging. *IEEE Transactions on Transportation Electrification, 7*(3), 1205–1218. https://doi.org/10.1109/TTE.2021.3049138

Peng, J., Zhang, B., & Su, W. (2025). A hybrid control strategy of LCC–LCC compensated electric vehicles wireless charging system with wide ZVS range. *IEEE Transactions on Power Electronics, 40*(4), 6282–6295. https://doi.org/10.1109/TPEL.2024.3516821

Pretorius, B. G., Strauss, J. M., & Booysen, M. J. (2024). Grid and mobility interdependence in the eventual electrification of operational minibus taxis in cities in sub-Saharan Africa. *Energy for Sustainable Development, 79*, Article 101411. https://doi.org/10.1016/j.esd.2024.101411

Ravi, S. S., & Aziz, M. (2022). Utilization of electric vehicles for vehicle-to-grid services: Progress and perspectives. *Energies, 15*(2), Article 589. https://doi.org/10.3390/en15020589

Rayan, B. A., Subramaniam, U., & Balamurugan, S. (2023). Wireless power transfer in electric vehicles: A review on compensation topologies, coil structures, and safety aspects. *Energies, 16*(7), Article 3084. https://doi.org/10.3390/en16073084

SAE International. (2024). *Wireless power transfer for light-duty plug-in/electric vehicles and alignment methodology* (SAE Standard J2954_202408). https://doi.org/10.4271/J2954_202408

Sagaria, S., van der Kam, M., & Boström, T. (2025). Vehicle-to-grid impact on battery degradation and estimation of V2G economic compensation. *Applied Energy, 377*, Article 124546. https://doi.org/10.1016/j.apenergy.2024.124546

She, X., Huang, A. Q., Lucia, O., & Ozpineci, B. (2017). Review of silicon carbide power devices and their applications. *IEEE Transactions on Industrial Electronics, 64*(10), 8193–8205. https://doi.org/10.1109/TIE.2017.2652401

Shi, B., Yang, F., Hu, C., & Ouyang, M. (2021). Modelling and improvement of oscillation problem in a double-sided LCC compensation network for electric vehicle wireless power transfer. *eTransportation, 8*, Article 100108. https://doi.org/10.1016/j.etran.2021.100108

Tang, Y., Hu, W., Xiao, J., Lu, Z., Li, Z., Huang, Q., Chen, Z., & Blaabjerg, F. (2022). RL-ANN-based minimum-current-stress scheme for the dual-active-bridge converter with triple-phase-shift control. *IEEE Journal of Emerging and Selected Topics in Power Electronics, 10*(1), 673–689. https://doi.org/10.1109/JESTPE.2021.3071724

Teodorescu, R., Blaabjerg, F., Liserre, M., & Loh, P. C. (2006). Proportional-resonant controllers and filters for grid-connected voltage-source converters. *IEE Proceedings – Electric Power Applications, 153*(5), 750–762. https://doi.org/10.1049/ip-epa:20060008

Thrimawithana, D. J., & Madawala, U. K. (2013). A generalized steady-state model for bidirectional IPT systems. *IEEE Transactions on Power Electronics, 28*(10), 4681–4689. https://doi.org/10.1109/TPEL.2012.2237416

Upadhyay, N., Padhy, N. P., & Agarwal, P. (2024). Grid-current control with inverter-current feedback active damping for LCL grid-connected inverter. *IEEE Transactions on Industry Applications, 60*(1), 1738–1749. https://doi.org/10.1109/TIA.2023.3316997

Venkatesan, M., Narayanamoorthi, R., AboRas, K. M., & Emara, A. (2024). Efficient bidirectional wireless power transfer system control using dual phase shift PWM technique for electric vehicle applications. *IEEE Access, 12*, 27739–27755. https://doi.org/10.1109/ACCESS.2024.3367437

Venkatesan, M., Rajamanickam, N., Vishnuram, P., Bajaj, M., Blazek, V., Prokop, L., & Misak, S. (2022). A review of compensation topologies and control techniques of bidirectional wireless power transfer systems for electric vehicle applications. *Energies, 15*(20), Article 7816. https://doi.org/10.3390/en15207816

Wang, X., Jiang, C. Q., Wang, Y., Chen, C., Zhou, J., & Luo, B. (2025). Analysis of triple phase shift strategy in wireless power transfer systems considering asymmetric parameters and harmonics for enhanced energy efficiency. *Energy, 333*, Article 137495. https://doi.org/10.1016/j.energy.2025.137495

Yanagi, T., Nakahara, K., Nagai, S., Shimizu, O., & Fujimoto, H. (2025). Optimizing the number of parallel SiC MOSFET chips in a wireless power transfer inverter with pulse width control. *IEEE Transactions on Industrial Electronics, 72*(9), 8995–9004. https://doi.org/10.1109/TIE.2025.3531459

Yilmaz, M., & Krein, P. T. (2013). Review of the impact of vehicle-to-grid technologies on distribution systems and utility interfaces. *IEEE Transactions on Power Electronics, 28*(12), 5673–5689. https://doi.org/10.1109/TPEL.2012.2227500

Younis, T., Al-Ismail, F. S., Amrr, S. M., & Hussain, S. M. S. (2025). Optimization strategies for triple-phase-shift modulation in dual-active-bridge converters: A comprehensive review. *IEEE Access, 13*, 152748–152761. https://doi.org/10.1109/ACCESS.2025.3603104

Zhang, Y., Fang, J., Gao, F., Song, T., Gao, S., & Rogers, D. J. (2020). Second-harmonic ripple voltage suppression of integrated single-phase pulsewidth modulation rectifier charging system for EVs. *IEEE Transactions on Power Electronics, 35*(4), 3616–3626. https://doi.org/10.1109/TPEL.2019.2937745

Zhang, Y., Li, X., Chen, S., & Tang, Y. (2022). Soft switching for strongly coupled wireless power transfer system with 90° dual-side phase shift. *IEEE Transactions on Industrial Electronics, 69*(1), 282–292. https://doi.org/10.1109/TIE.2021.3055158

Zhao, B., Song, Q., & Liu, W. (2012). Power characterization of isolated bidirectional dual-active-bridge DC–DC converter with dual-phase-shift control. *IEEE Transactions on Power Electronics, 27*(9), 4172–4176. https://doi.org/10.1109/TPEL.2012.2189586

Zhao, B., Song, Q., Liu, W., & Sun, Y. (2014). Overview of dual-active-bridge isolated bidirectional DC–DC converter for high-frequency-link power-conversion system. *IEEE Transactions on Power Electronics, 29*(8), 4091–4106. https://doi.org/10.1109/TPEL.2013.2289913

Zmood, D. N., & Holmes, D. G. (2003). Stationary frame current regulation of PWM inverters with zero steady-state error. *IEEE Transactions on Power Electronics, 18*(3), 814–822. https://doi.org/10.1109/TPEL.2003.810852